RESEARCH ARTICLE

Key Points:

- We develop a reduced model that can generate small-scale rich submesoscale-like flows in two-dimensions
- The model can generate flows with a forward energy cascade, enhanced small scale dissipation, and cyclone-anticyclone asymmetric vortices
- The model generated flows compare qualitatively well with realistic submesoscale flows, making it useful for variety of applications

S-2DV: A New Reduced Model Generating Submesoscale-Like Flows

Krithin Gowthaman[1] and Jim Thomas[1,2]

[1]International Centre for Theoretical Sciences, Tata Institute of Fundamental Research, Bangalore, India, [2]Centre for Applicable Mathematics, Tata Institute of Fundamental Research, Bangalore, India

Abstract Oceanic mesoscale flows are characterized by an inverse kinetic energy cascade and the subsequent formation of large coherent vortices, and these flow features are captured well by the quasi-geostrophic (QG) model. Oceanic submesoscale flow dynamics are however significantly different from those of mesoscales. The increase in unbalanced energy levels and the Rossby number at submesoscales results in cyclone-anticyclone asymmetry in vorticity structures, forward kinetic energy cascades, and enhanced small-scale dissipation. In this paper, we develop a reduced single-equation model that can generate submesoscale-like flows in two dimensions. We start from the two-dimensional barotropic QG equation and add an external random vorticity field, to mimic the effect of unbalanced flow components. Thereafter, we add a vorticity-squared term, to generate asymmetry in the vorticity structures. By varying the strength of these two terms, we observe that the model can generate submesoscale-like flows that compare qualitatively well with realistic flows generated by complex ocean models. The reduced model is seen to be capable of generating flows that are intermittent in nature, are characterized by a forward energy flux, and are composed of small-scale flow structures along with enhanced energy dissipation. We further demonstrate the practical utility of the model by applying it to a passive tracer dispersion and a plankton patchiness problem, these being applications that require submesoscale-like flows. Our investigation points out that the new model could serve as a convenient platform for various applications that require submesoscale-like flows, such as testing and developing different kinds of parameterizations.

Plain Language Summary Oceanic flows span several decades of spatial scales with the flow dynamics varying significantly across different scales. The lack of a self-similar behavior of the flow at different scales and the limited computational resources make it challenging to capture all relevant scales through numerical simulations of the governing equations. This necessitates the development of reduced models capable of generating flows that resemble oceanic behavior at various scales. Over the past two decades, oceanographic research has highlighted the significance of the submesoscale flows which are roughly a decade smaller than the mesoscales, making them challenging to resolve in coarse-resolution ocean models. In this work, we develop a two-dimensional reduced model by modifying the simplest version of the widely used quasi-geostrophic equation, to capture multiple features of submesoscale flows. The flows generated by the new model qualitatively compare well with submesoscale flows generated by complex ocean models. The new model could be used to generate submesoscale-like flows for various applications, as demonstrated by applying it to passive tracer dispersion and a plankton patchiness problem in the ocean.

1. Introduction

Oceanic mesoscale flows, with $\mathcal{O}(50)$ km horizontal scales, are dominated by coherent eddies that carry almost 90% of the flow kinetic energy (Chelton et al., 2011; Ferrari & Wunsch, 2009). The smallness of Rossby number and Froude number at these scales, as a result of rapid rotation and strong stratification, leads to quasi-two-dimensionalization of the flow. These conditions lead to the applicability of the quasi-geostrophic (QG) equation, a reduced single-equation model, to capture the dynamics of mesoscale flows (R. B. Scott & Wang, 2005; Vallis, 2006). Similar to the two-dimensional vorticity equation, the QG equation is characterized by an inverse energy cascade, forming large coherent vortices that can get bigger with time via vortex mergers.

Although the QG equation is a robust reduced model for capturing the balanced flow dynamics in the small Rossby number regime, the presence of unbalanced flow components limits the regime of validity of the model, especially at submesoscales. In this work, we use the term "submesoscale" broadly to include scales where the
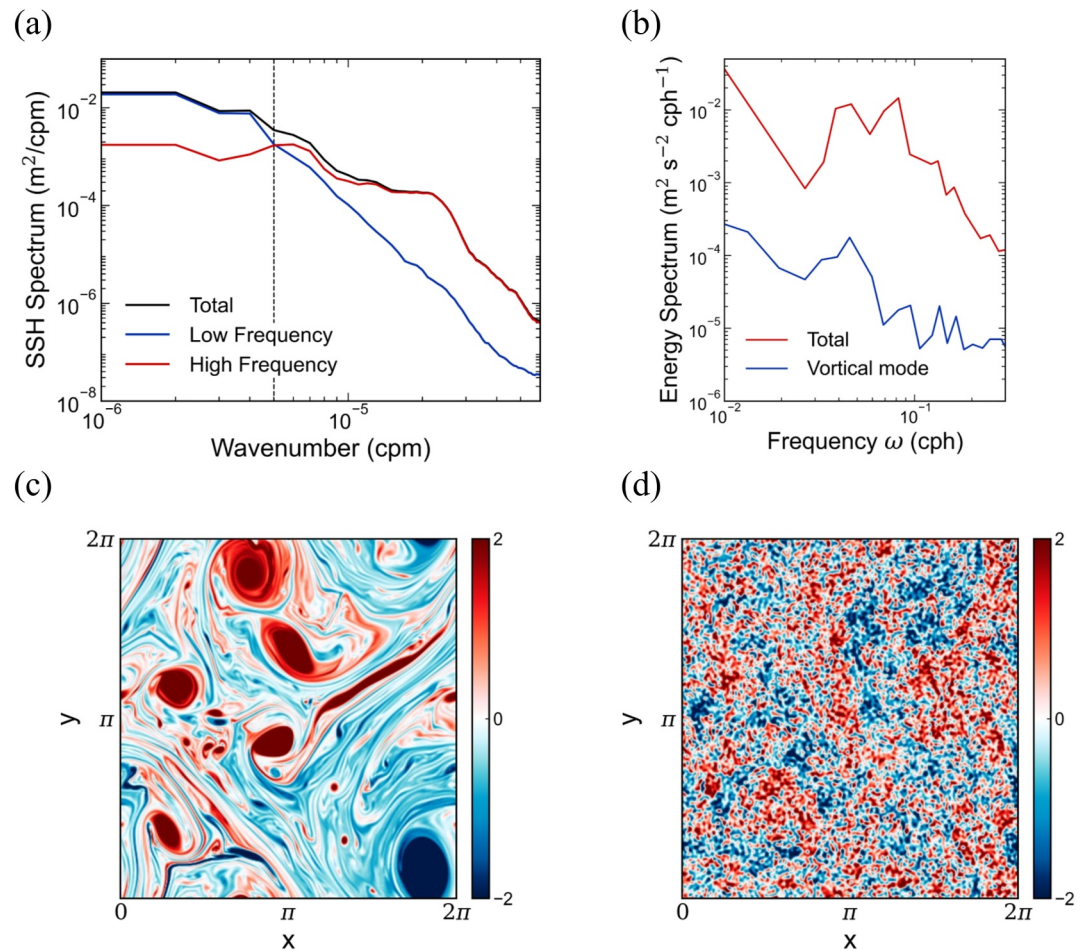
Figure 1. Panel (a), adapted with permission from Richman et al. (2012) copyright 2012 John Wiley and Sons, shows the sea surface height spectrum in wavenumber space obtained from global-scale ocean model simulation based results. Panel (b) shows the energy spectrum in frequency space based on in situ measurements, this figure being adapted from Thomas (2023) and the oceanic regime being detailed in Lien and Sanford (2019). Bottom row shows physical structure of the geostrophically balanced mode's vertical vorticity field from results discussed in Thomas and Daniel (2021). The panels show results for a flow composed of (c) balanced flow and insignificant internal waves and (d) strong internal waves and weak balanced flow.

flow cannot be described by the balanced component alone. This broad definition allows us to consider both low Rossby number flows dominated by internal gravity waves and $\mathcal{O}(1)$ Rossby number flows under the umbrella of the term "submesoscale."

To highlight flow features across scales, Figure 1 shows the changes in the flow dynamics as we move from mesoscales to submesoscales in the ocean. Specifically, Figure 1a is taken from Richman et al. (2012) and shows the sea surface height spectrum from a global scale model output. Notice that the high frequency (HF) red curve overtakes the low frequency blue curve before the 100 km (10^{-5} cpm) scale. Similarly, Figure 1b based on in situ data sets discussed in Lien and Sanford (2019), shows the balanced or the vortical spectrum (blue curve) being much weaker than the wave spectrum, the latter almost equaling the total spectrum (red curve). Over the past two decades, a large collection of ocean model outputs, in situ measurements, and satellite data sets have pointed out results similar to those seen in Figures 1a and 1b: that is, internal wave energy levels start dominating over balanced flow energy levels below a certain transition scale, which can vary from $\mathcal{O}(10) - \mathcal{O}(100)$ kms in the many regions in the world's oceans (Callies et al., 2015; Cao et al., 2019; Lien & Sanford, 2019; Pinkel, 2014; Qiu et al., 2017, 2022; Savage et al., 2017; Tchilibou et al., 2018; Torres et al., 2018; Vladoiu et al., 2024; Yu, Ponte, et al., 2019). The bottom row of Figure 1, based on results discussed in Thomas and Daniel (2021), obtained by the numerical integration of the Boussinesq equations, shows the difference in balanced flow dynamics at scales

larger than the transition scale (where waves are weak compared to balanced flow, panel c) and at scales smaller than the transition scale (where waves are stronger than balanced flow, panel d). While the QG model can generate the flow in Figure 1c that is composed of domain-scale coherent vortices, the reduced model is incapable of capturing small-scale rich flows such as that shown in Figure 1d, where flow dynamics are severely affected by the presence of energetic internal waves.

In addition to the scenario sketched above, where QG dynamics fail to apply at scales where wave energy levels surpass balanced flow energy, oceanic flows whose Rossby number approaches $\mathcal{O}(1)$ values are also characterized by notable departure from QG model-based results (Brannigan et al., 2015; Capet et al., 2008b; Poje et al., 2017; Shcherbina et al., 2013; Siegelman et al., 2020; Thomas & Vishnu, 2022; Thompson et al., 2016; Yu, Naveira Garabato et al., 2019). These flows are characterized by energetic small scale vortices, forward flux of energy, and cyclone-anticyclone asymmetry in the vortical structures. In either scenario—where the flow Rossby number approaches $\mathcal{O}(1)$ values or when internal wave energy levels are high relative to the balanced flow energy—QG model becomes unreliable, necessitating the return to models of higher levels of complexity, such as the Boussinesq equations (Thomas, 2023). Handling this complexity becomes inevitable due to the need to resolve and model the unbalanced flow components explicitly, to capture its effect on balanced dynamics.

When it comes to applications such as predicting the trajectories of Lagrangian particles, tracer dispersion, marine ecosystem dynamics etc, one cannot overstate the utility of simplified flow models that can generate complex flow structures. Recognizing this, a multitude of flow-generating techniques have been in use for a variety of applications. The simplest among these are the kinematic flow models, where a velocity field is constructed with random Fourier modes following a known probability distribution (Kraichnan, 1970). Such kinematic models could be designed to generate more complex fields by making the Fourier modes evolve according to certain stochastic differential equations, while enforcing some level of correlation over time. Meacham and Berloff (2023) used this strategy to study clustering of particles in the upper ocean. Flow generators may also be built by incorporating a stochastic field within a deterministic model to simulate complex features of turbulent flows. Li et al. (2023) applied this approach, parameterizing unresolved eddy effects using a time-varying small-scale velocity field while conserving energy. Pushing beyond such kinematic flows, the surface quasi-geostrophic equation is a single-equation model that can generate small submesoscale-like features (Lapeyre, 2017). Various adaptations of this model have been used to generate realistic flows in the upper and interior regions of the ocean (Lapeyre & Klein, 2006; Wang et al., 2013; Yassin & Griffies, 2022). The semi-geostrophic model applies in frontal regimes and retains the full ageostrophic velocity in the advection term. As a result, the semi-geostrophic model goes beyond some of the restrictive assumptions of the standard QG model and can generate flows with more realistic submesoscale features (Hoskins & Bretherton, 1972; Ragone & Badin, 2016). Another example is the hypo-geostrophic model derived by McWilliams and Gent (1980), which goes beyond geostrophy by asymptotically incorporating higher-order terms in the equation, aiming to capture unbalanced flow effects.

Instead of reverting to the full Boussinesq equations, one can develop reduced models that retain the dominant wave mode and vortical dynamics while being less complex. This strategy is particularly advantageous for capturing geophysical flows with energetic inertia-gravity wave fields interacting with balanced flow. In this context, Thomas and Yamada (2019), Thomas and Arun (2020), and Thomas and Vishnu (2022) developed reduced models by projecting the hydrostatic Boussinesq equations onto the barotropic and a single baroclinic mode for examining wave-balance and fast-slow exchanges across various parameter regimes. These two-vertical-mode models capture both wave and balanced modes, are two-dimensional in nature, and are handy for long term high-resolution numerical integrations with affordable computational resources. These models also capture the essential features of submesoscale dynamics, such as forward energy flux and the formation of energetic small-scale structures, making them versatile for different applications. For instance, Thomas and Gupta (2022) and Sirohi and Thomas (2024) used these two-vertical-mode models to demonstrate how effects induced by inertia-gravity waves and submesoscale flows can enhance tracer dispersion.

Keeping in view the significant changes the flow structures undergo as we move from mesoscales to submesocales, as detailed above, this paper presents a two-dimensional flow model that can capture the turbulent transitions across scales. To achieve this, we modify the simplest version of the QG equation: the barotropic QG equation or the two-dimensional vorticity equation, by introducing a random external vorticity field in the model to mimic unresolved unbalanced modes. Furthermore, we introduce a second modification to introduce cyclone-anticyclone asymmetry in the model. The combined effect of these modifications captures several key features

observed in realistic submesoscale flows, akin to more complex models. Specifically, the new parameterized model evidently captures some of the crucial features that are seen in submesocale flows, such as a forward energy flux, energetic small-scale structures, and enhanced small-scale dissipation.

The plan for this paper is as follows: we present the new model and its features in Section 2, discuss features of flows generated by the model in Section 3, compare flows generated by the model with complex submesoscale flows discussed in multiple previous studies in Section 4, demonstrate the utility of the new model for two oceanographic application problems in Section 5, and summarize our findings in Section 6.

2. The Model and Its Features

To begin with, we recall the barotropic QG, two-dimensional Euler equation, or the two-dimensional vorticity (2DV hereafter) equation

$$\frac{\partial Q}{\partial t} + \partial[\psi, Q] = 0, \quad Q = \Delta\psi \tag{1}$$

where Q is the potential vorticity (PV), which is also the vorticity field for 2DV, ψ is the streamfunction, $\Delta = \partial^2/\partial x^2 + \partial^2/\partial y^2$ is the Laplacian operator, and the Jacobian is defined as $\partial[f, g] = \partial f/\partial x \, \partial g/\partial y - \partial f/\partial y \, \partial g/\partial x$. The velocity field is obtained from the streamfunction as $v = (u, v) = (-\partial\psi/\partial y, \partial\psi/\partial x)$.

2DV, Equation 1, is a special case of the single-layer shallow-water QG equation in the limit of infinite deformation length. We can also obtain 2DV by constraining the three-dimensional QG equation to the barotropic mode alone, hence the name barotropic QG equation. The model, as written in Equation 1, captures the turbulent dynamics of the vortical mode. If we modify Q to incorporate the differential rotation effect using the β-plane approximation as $Q = \Delta\psi + \beta y$, the model becomes capable of supporting dispersive Rossby waves in addition to vortical dynamics (Salmon, 1978; Vallis, 2006). Without these additional terms, the 2DV model in Equation 1 is one of the simplest mathematical models that can generate geophysical turbulent flows.

The turbulent dynamics of 2DV are characterized by an inverse energy flux, that is, energy gets transferred from small scales and accumulates at large domain scales, in the form of coherent vortices that resemble mesoscale eddies in the ocean. In contrast, submesoscale flows are characterized by a forward energy flux. Our goal is to modify 2DV so that the modified model has tunable parameters, making it capable of generating small-scale rich flows with a forward energy flux as parameters are varied. For this, we draw inspiration from next-order approximations to the QG equation derived in past studies, such as Allen (1993), Muraki et al. (1999), Zeitlin et al. (2003), and Thomas (2023). Specifically, Equation 2.6 in Thomas (2023) is an asymptotic equation for the PV field written as

$$\frac{\partial Q}{\partial t} + \partial[\psi, Q] = 0 \tag{2a}$$

$$Q = Q_G + Ro\ Q_{GG} + Ro\ Q_{WW}, \quad \psi = \psi_G + Ro\ \psi_{GG} + Ro\ \psi_{WW} \tag{2b}$$

Above, Ro is the Rossby number, and Equation 2 is derived in the asymptotic limit $Ro \ll 1$. Setting $Ro = 0$ above gives us the standard QG equation. Q_{GG} refers to quadratic nonlinear balance-balance interaction terms. A higher-order balanced equation that includes these balance-balance interaction terms, but discards waves, is detailed in Zeitlin et al. (2003). Numerical integrations of such higher-order balanced models by Rotunno et al. (2000) and Hakim et al. (2002) showed that incorporating these balance-balance interaction terms into the dynamics can lead to flows with cyclone-anticyclone asymmetry. Q_{WW} refers to quadratic nonlinear wave-wave interaction terms. These terms are responsible for reversing the geostrophic energy cascade from inverse to forward when the flow is rich with high energy waves, as shown using numerical integrations in Thomas and Daniel (2021).

In this paper, we avoid a detailed term-by-term discussion of Equation 2 and its derivation, for which we refer the reader to Thomas (2023). We note that such models are slow evolution equations for the balanced dynamics, and they are not closed since wave-wave interaction terms appear in the equation. Closure requires coupling equations like Equation 2 with the evolution equation for waves. Alternatively, if we parameterize the effect of waves, we

would have a single evolution equation for the balanced flow without having to evolve a separate equation for waves. Aiming to develop a single-equation model for the slow dynamics, we parameterize the effect of waves with a random field that is prescribed a priori and use this to modify 2DV as

$$\frac{\partial Q}{\partial t} + \partial[\psi, Q + Q_s] = 0, \quad Q = \Delta\psi \tag{3}$$

where Q_s is the externally imposed random field with "s" denoting submesoscale. Although we are inspired by Equation 2, which includes wave contributions, we treat Q_s as a parameterization for all kinds of submesoscale flow components, including internal waves and other unbalanced flow components. In this work, we identify equations of the above form, where an external term parameterizing submesoscale effects is introduced into the Jacobian term, as Submesoscale-2DV or S-2DV.

In general we could let Q_s change with time, making it a stochastic term—a random field that evolves with time. Although we experimented with time varying Q_s, we found that the flows generated were qualitatively similar to those obtained by incorporating a stationary-in-time Q_s field in S-2DV. Consequently, in this paper, we will focus on the case where Q_s has no time-dependence, thereby parameterizing all the unbalanced effects as "frozen-in-time." For this special case, Equation 3 has material conservation of $Q + Q_s$, since the time derivative of Q_s vanishes. Moreover, when Q_s has no time-dependence, the mathematical form of Equation 3 is similar to that of barotropic QG equation in the presence of a topography, where Q_s resembles the mathematical term representing topography (Hart, 1979; Holloway, 1987). Despite this setup, as will be shown below, the stationary-in-time Q_s field in S-2DV can still lead to the generation of high-frequency small-scale-rich flows.

Comparing Equations 2 and 3, notice that we introduced a modification to the PV field in the Jacobian, without modifying the streamfunction field. As will become clear below, this form of Equation 3 allows the model to conserve energy, which inspired the choice. Nevertheless, it is important to emphasize that, unlike Equation 2, which can be derived through a systematic asymptotic procedure, Equation 3 is an ad hoc model. While mathematical insights from asymptotic models and some physical insights regarding conservation laws, as detailed below, inspired the form given in Equation 3, it is worth noting that this reduced model is not derived through any systematic procedure. Consequently, the fruitfulness of this model will be judged based on the nature of the flows it generates, comparisons of such flows with those generated by more complex realistic models, and by using these flows for relevant applications.

2.1. Conservation Laws

The introduction of the term Q_s leads to changes in the conservation laws in comparison to 2DV. Multiplying Equation 3 by ψ and integrating over the domain (D) gives us the energy equation

$$\frac{dE}{dt} = \frac{d}{dt}\int_D \frac{1}{2}(\nabla\psi)^2 d\boldsymbol{x} = -\int_D \psi\partial[\psi, Q + Q_s]\,d\boldsymbol{x} = -\int_D (Q + Q_s)\partial[\psi, \psi]d\boldsymbol{x} = 0 \tag{4}$$

where $\boldsymbol{x} = (x, y)$. The above equation shows us that Equation 3 conserves energy, with the expression for energy being the same as the one for Equation 1.

As mentioned earlier, if we had incorporated a modification to the streamfunction field in the Jacobian term in 2DV, we would not have obtained the energy conservation for the model. For this reason, we modified the PV field without changing the streamfunction in 2DV to get Equation 3.

Similarly, multiplying Equation 3 by Q and integrating over the domain gives us the enstrophy evolution equation

$$\frac{d\mathcal{E}}{dt} = \frac{d}{dt}\int_D \frac{1}{2}Q^2 d\boldsymbol{x} = -\int_D Q\partial[\psi, Q + Q_s]\,d\boldsymbol{x} = \int_D \psi\partial[Q, Q_s]\,d\boldsymbol{x} \tag{5}$$

In the absence of the term Q_s, the last term above would be zero, implying enstrophy conservation. However, for non-zero Q_s, enstrophy is not conserved by Equation 3.

The above discussion highlights the major change in conservation laws of S-2DV when compared to 2DV. The original model, 2DV, conserves energy E and enstrophy $\mathcal{E}$, with this dual conservation law set being responsible for the dual cascades: the inverse cascade of energy and the forward cascade of enstrophy (Salmon, 1978; Vallis, 2006). In contrast, S-2DV, like the Boussinesq equations, conserves energy but does not conserve enstrophy. Consequently, a forward cascade of energy might be seen in S-2DV, a hypothesis which we will test using numerical integrations in the next section.

2.2. Constructing a Random Vorticity Field

We associate a streamfunction ψ_s with the random vorticity field Q_s as

$$Q_s = \Delta \psi_s \tag{6}$$

and define the random field's energy, similar to the flow energy expression as

$$E_s = \int_D \frac{1}{2} (\nabla \psi_s)^2 d\boldsymbol{x} = \sum_k k^2 |\hat{\psi}_s(k)|^2 = \sum_k \hat{E}_s(k) \tag{7}$$

To construct the random vorticity field, we first generated a two-dimensional complex random array $\hat{\psi}_s(\boldsymbol{k})$ drawn from the standard Gaussian distribution, where the wavenumber vector $\boldsymbol{k} = (k_x, k_y)$. We then scaled the elements of this array so that the energy computed using this array $\hat{E}_s(k)$ had the following form, with pre-specified positive real numbers a and b:

$$\hat{E}_s(k) = ak^{-b} \tag{8}$$

where $k = \sqrt{k_x^2 + k_y^2}$ is the wavenumber vector magnitude. As noted above, a is a scaling factor that controls the energy level of the externally imposed random perturbation term while b sets the slope of the energy spectrum associated with the same term. Recall that one of our goals is to produce three-dimensional submesoscale-like features in our two-dimensional system, and $k^{-5/3} - k^{-2}$ is an inertial range energy spectral scaling that is often seen at submesoscales (Brannigan et al., 2015; Callies et al., 2015; Cao et al., 2019; Capet et al., 2008b; Qiu et al., 2017; Rocha, Chereskin, et al., 2016; Tchilibou et al., 2018; Vladoiu et al., 2024). After some experimentation, we found that the $b = 2$ case generated turbulent fields that were not very different from $b = 5/3 \approx 1.7$ case. Consequently, we will present results obtained by setting $b = 2$.

Using the above definitions of the flow energy E and the random field's energy E_s, we quantify the relative strength of the random vorticity field with the parameter $R = E_s/E$. As the reader might guess, a low R value would mean weak random external field and therefore negligible changes may be expected to the turbulent dynamics from that predicted by 2DV. On the other hand, a high R value can lead to significant changes in the flow dynamics when compared to the flow generated by 2DV.

We employed the aforementioned means to generate the external pre-specified vorticity field, ζ_s, to be used in Equation 3. Once a certain ζ_s is generated, it remains constant during the entire flow evolution, since we do not let the external field have time-dependence. As is usually followed in turbulent flow-generation algorithms, we chose random numbers to construct the external field ζ_s to avoid unintentionally enforcing any specialized features on the field. Specifically, each wavenumber of the random field in Fourier space had the form $\zeta_s(\boldsymbol{k}) = \alpha_{\boldsymbol{k}} e^{i\beta_{\boldsymbol{k}}}$, where the amplitude $\alpha_{\boldsymbol{k}}$ and phase $\beta_{\boldsymbol{k}}$ were random variables. Nevertheless, on experimenting with a wide range of random fields, we found that the relative strength of the random field, dictated by R, had a major effect on the flow while the random numbers that made up the field had little significance. More precisely, different random fields that had the same a and b in Equation 8, resulting in the same R, generated similar flow fields with the S-2DV model. These experiments confirm that users of S-2DV may use arbitrary random fields to generate similar flows, as long as the relative strength of the external term is the same.

2.3. Numerical Integration Details

We time-stepped S-2DV, Equation 3, using the fourth-order Runge-Kutta method and Fourier pseudospectral method with 2/3 dealiasing over a doubly periodic domain, $[x, y] \in 2\pi \times 2\pi$. While the S-2DV model can be integrated with different boundaries in place, we used periodic boundary conditions in this work for convenience and to obtain high-accuracy solutions of the model using spectral basis. We generated solutions at spatial resolutions of 384^2, 576^2, and 768^2 with fourth-order Runge-Kutta time-stepping scheme. Below, we present results from the highest resolution integrations with 768^2 grid points, where both the flow and associated statistics numerically converged.

We forced S-2DV at low wavenumbers $k \leq 2$ and maintained the energy in the low wavenumbers at all times. We achieved this using the forcing scheme detailed in Thomas and Vishnu (2022). A particular advantage of this forcing scheme is that it does not force energy into the system at a pre-specified rate. Instead, if the flow undergoes a forward energy cascade resulting in the transfer of energy to smaller scales, the forcing mechanism injects energy into the low-wavenumber band proportionally, to maintain the large-scale energy lost to small scales. Conversely, if there is no transfer of energy to smaller scales, the forcing shuts off, not injecting energy into the system. Such a forcing scheme is beneficial since it injects energy into the large scales based on the rate of transfer of energy from large scales to small scales and not based on a pre-set injection rate. We specifically used this forcing scheme in the present study since we do not know the rate of forward cascade and downscale energy transfer at different R beforehand, and therefore did not want to externally enforce an energy injection rate.

In addition to the forcing, we added the hyperdissipative term $-\nu\Delta^8 Q$ on the right hand side of Equation 3, to dissipate energy reaching grid scale without any accumulation. For the resolution of 768^2 grid points, we set the hyperviscosity $\nu = 10^{-38}$. Using hyperdissipation, as opposed to the regular dissipation term $\nu\Delta Q$, allows us to have an extended inviscid inertial range that is unaffected by viscous effects. To corroborate the effectiveness of the hyperdissipative operator, we have provided a comparison between the regular and hyper dissipative numerical simulations in terms of their energy spectra: see Figure S1 and its description in Supporting Information S1.

We initialized the vorticity fields from a standard Gaussian distribution at low wavenumbers, $k \leq 2$, in spectral space. Based on the aforementioned forcing scheme, we found that flows generating numerous small-scale structures that got dissipated required high-energy forcing, while flows dominated by large-scale coherent vortices extracted minimal energy from the forcing, rendering the forcing strength negligible. Each numerical integration was performed until the energy and various other statistical quantities, reported below, reached equilibrated states. All integrations reached an equilibrium before $t = 300$, although we continued them up to $t = 2000$ and used data from the time window $t = 500 - 2000$ for all analyses discussed in the results section below. We generated numerical solutions for a few hundred R values, with R ranging from 10^{-7} to 1, and found that extremely low values of R resulted in solutions similar to those generated by 2DV. Therefore, we selected 29 flows whose R values ranged from $R = 1.8 \times 10^{-5}$ to $R = 1$ and present corresponding results in the following section.

3. Results

Based on a broad set of numerical integrations, Figure 2 shows vorticity fields normalized by their root-mean-square (RMS) values for four different R values: $R_1 = 1.8 \times 10^{-5}$, $R_2 = 7 \times 10^{-3}$, $R_3 = 0.11$ and $R_4 = 1$. Observe that for the lowest R case, the R_1 flow shown in Figure 2a, consists of domain-scale coherent vortices with minimal small-scale structure, while increasing R shows the presence of fine-scale vorticity structures, as seen in Figures 2b and 2c. In the highest R value case, the R_4 flow, coherent vortices are almost entirely broken down. A reader carefully examining Figure 2d will find bits and pieces of coherent vortices that form the skeleton of the flow: for example, see the red-colored broken pieces of a coherent vortex roughly in the center of the domain in Figure 2d. The transition seen in Figures 2a–2d is qualitatively similar to what is expected in the world's oceans, as we move from large rotation-dominated quasi-two-dimensional scales to small fully three-dimensional scales where the effects of rotation weaken. With further increase in R, we found that all remnants of coherent structures disappeared from the flow field (see Figure S2 in Supporting Information S1). The flow at large R values, $R \gg 1$, was seen to be composed of a homogeneous distribution of small-scale structures, resembling three-dimensional homogeneous isotropic turbulent flow fields.
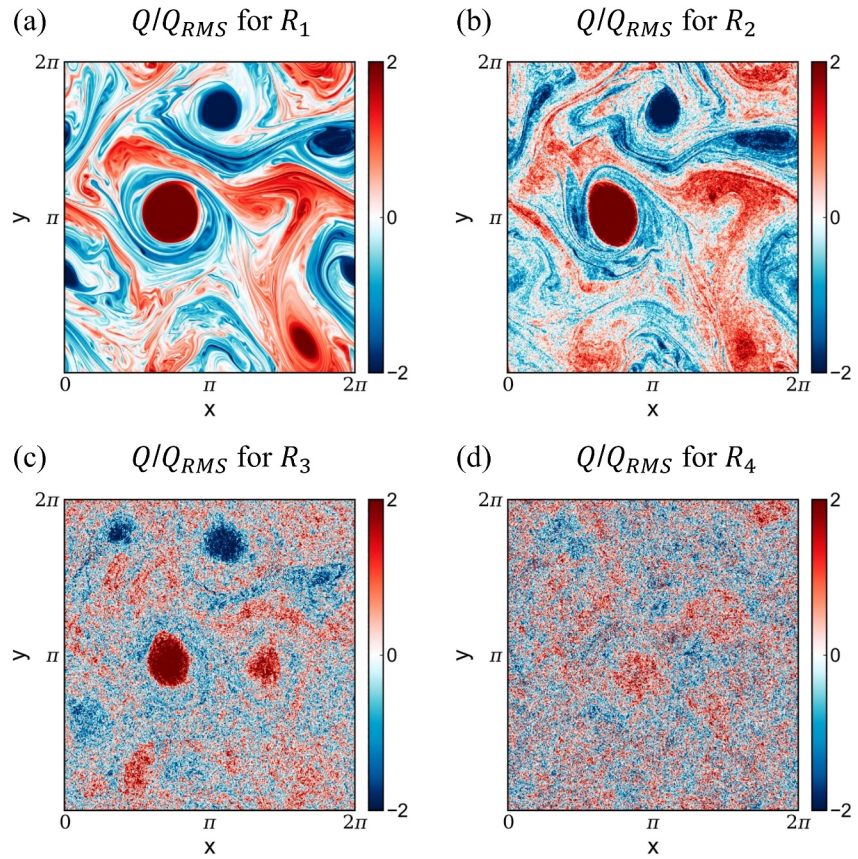
Figure 2. Vorticity fields normalized by their RMS values for the four flows with R values (a) R_1, (b) R_2, (c) R_3, and (d) R_4.

The energy spectra of the four flows mentioned above are shown in Figure 3a, revealing the effect of increasing small-scale structures in the flow with increasing R. The R_1 flow's spectrum is steeper than k^{-3}, owing to the flow being rich with domain-scale coherent vortices. Meanwhile, the spectra of higher R flows are shallower, with the spectra of R_3 and R_4 being k^{-2}, the same as that of the external field's energy spectrum $\hat{E}_s(k)$. Notably, by gradually increasing R, the flow spectrum can be made to approach a desired spectral slope by enforcing an external vorticity field Q_s whose energy spectrum $\hat{E}_s(k)$ has the desired slope. Similarly, we were able to obtain other desired slopes, such as $k^{-1.5}$, $k^{-1.7}$, $k^{-2.1}$ etc, for the flow spectrum by appropriately choosing the external field in S-2DV. Despite this behavior, it is important to not conflate the flow generated by S-2DV with the externally imposed random field, Q_s. While the former is a dynamically evolving flow with coherent vortices merging or disintegrating with time, the latter is a fixed-in-time uncorrelated random field with no dynamical features. To give a specific example, the R_3 flow in Figure 2c has coherent vortices floating in a background composed of broken bits and pieces of vorticity fragments and has an energy spectrum slope of k^{-2}, while the frozen-in-time random field Q_s with k^{-2} energy spectrum has no comparable features.

Similar to the shallowing of the energy spectra with increasing R, we found that the frequency spectra also became shallower with increasing R. This can be seen in Figure S3 in Supporting Information S1, that shows the frequency spectra of the lowest (R_1) and highest (R_4) R-flows. Therefore, with increased generation of small-scale features in the flow with shallower energy spectra, we end up with flows with more energy at higher temporal frequencies.

We now turn our attention to examining the energy fluxes across the scales. For this, temporarily ignoring the forcing and dissipative terms, we multiply the Fourier transform of Equation 3 with the complex conjugate of the Fourier transform of the streamfunction ψ and take the real part of the equation so obtained. This equation is then summed from the maximum wavenumber, $k_{\max}$, to an arbitrary wavenumber k to get the equation for the evolution of the energy contained in the wavenumber band $[k, k_{\max}]$ as
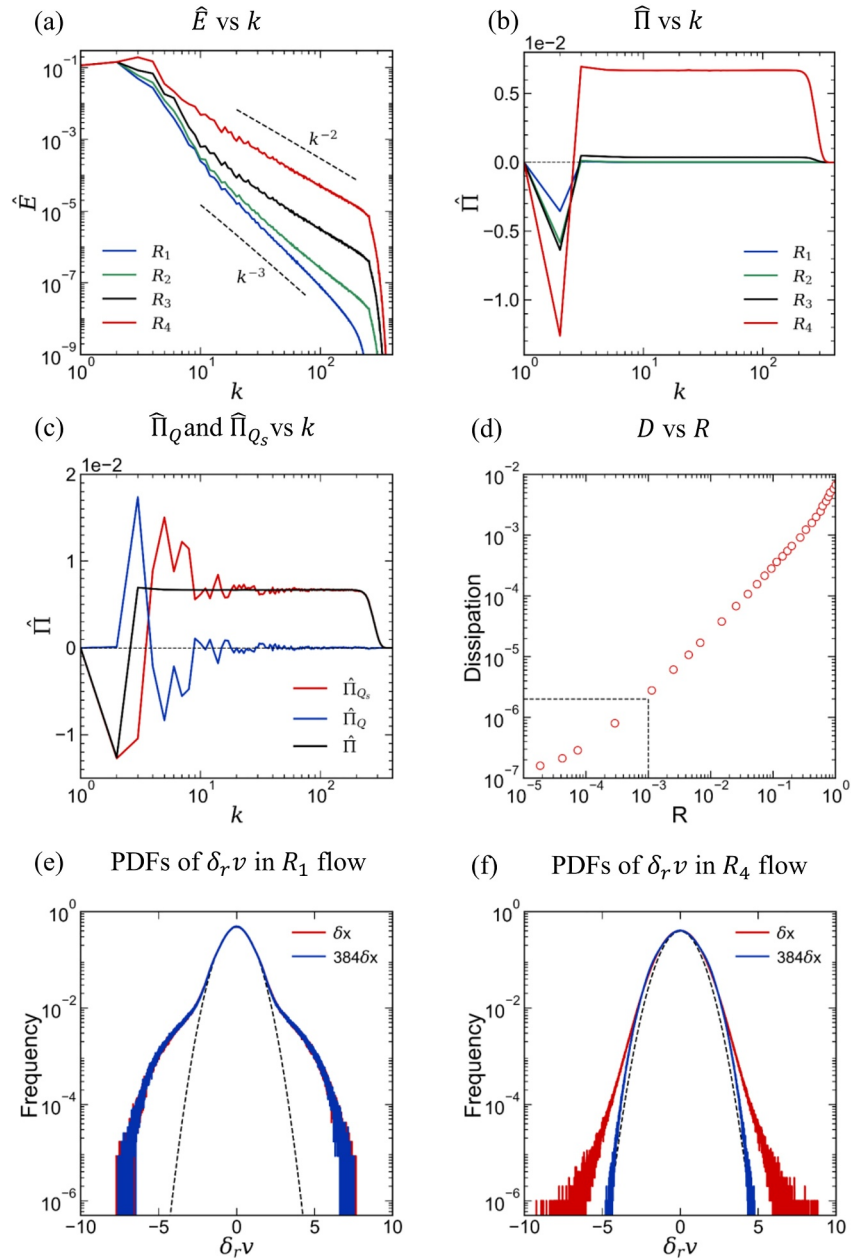
Figure 3. (a) Energy spectra for the four flows across R. (b) Comparison of spectral energy flux for different R flows. The horizontal black dashed line is used to highlight zero-flux line, helping to easily identify the sign of the flux for different cases. (c) Splitting of the total energy flux into its components. (d) Variation of flow energy dissipation with R. The region inside the black dashed lines is a region where the presence of the external field has negligible effect on the flow. Probability density functions of velocity distribution structure-functions normalized by their standard deviations for (e) R_1 flow and (f) R_4 flow. The dashed black curves in panels (e) and (f) represent the standard normal distribution.

$$\frac{d}{dt} \sum_{p=k_{\max}}^{k} \hat{E}_p = \hat{\Pi}(k,t) = \hat{\Pi}_Q(k,t) + \hat{\Pi}_{Q_s}(k,t) \qquad (9)$$

Above, $\hat{\Pi}$ is the total energy flux, which we decompose into contributions from two different terms. The first term, $\hat{\Pi}_Q$, arises from the product of ψ with the $\partial[\psi, Q]$ term in Equation 3 in Fourier space and is the flux term identical to the total flux term that arises in 2DV, Equation 1. The second term, $\hat{\Pi}_{Q_s}$, comes from the product of ψ with the

$\partial[\psi, Q_s]$ term in Equation 3 in Fourier space and is the result of the inclusion of the external field, having no equivalent term in Equation 1. Figure 3b shows the flux $\hat{\Pi}$ for the four different R values discussed earlier. For low R flows we see that the inertial range, $k \sim 10 - 100$, has almost zero flux, while for the high R flows we see a clear positive flux. Specifically, for the highest R flow, R_4, we see that the forward flux is the strongest (red curve). This flux for the R_4 flow is further decomposed into the two components given in Equation 9, shown in Figure 3c. Notice that the default flux term, $\hat{\Pi}_Q$ (blue curve), fluctuates at low wavenumbers and is negligible in the inertial range, specifically for $k > 10$. In contrast, $\hat{\Pi}_{Q_s}$ (red curve) takes high positive values throughout the inertial range, this being the cause for the high positive flux of $\hat{\Pi}$ in Figure 3b.

The features of the energy flux described above in the S-2DV model have qualitative similarities with energy flux seen in more complex models. Turbulent flow energy fluxes in a broad set of studies point out that on decomposing the energy flux into contributions from the balanced vortical mode and unbalanced wave and submesoscale modes, the flux term composed exclusively of the balanced modes does not contribute to the forward energy flux; it typically induces an inverse energy flux. The remaining cross-flux term involving balance and unbalanced contributions, is almost entirely responsible for the forward energy flux. This feature can be seen in Figure 8 in Capet et al. (2008a), Figure 3 in Delpech et al. (2024), Figure 6 in Tedesco et al. (2024), Figure 10 in Srinivasan et al. (2023), Figure 4d in Thomas and Daniel (2021), Figure 5c in Thomas and Vishnu (2022), and Figure 8 in Thomas and Arun (2020). It is noteworthy that the result seen in Figure 3c is strikingly similar to those seen in multiple previous studies listed here, indicating that the external random field is effective in incorporating the unbalanced flow effects into a balanced model (2DV), to provide us with a reduced model, S-2DV, that captures the effect of complex features that are not directly modeled.

We now look at the small scale dissipation of S-2DV. Dissipation is calculated by multiplying the dissipative term, $-\nu\Delta^8 Q$, by the streamfunction and integrating over the whole domain. The magnitude of this dissipation as a function of R is shown in Figure 3d. Concomitant with the results seen in earlier figures, increasing R generates more small-scale structures and a stronger forward cascade, resulting in a monotonic increase in dissipation with R; this being clear from Figure 3d. The black dashed lines in the figure are marked to identify the values of R greater than which the presence of the external field starts to impact the flow. Noticeable small scale dissipation and disruption of coherent vortices is seen for $R > \mathcal{O}(10^{-3})$.

To further examine the properties of flows generated by S-2DV, we looked for signs of intermittency in the flows. For this we used the velocity structure-function $\delta_r v$ defined as

$$\delta_r v = (v(x + r) - v(x)).\hat{r} \tag{10}$$

which is essentially the velocity difference between points separated by r, with the unit vector in this direction being indicated as $\hat{r}$. We examined the probability density functions (PDFs) of $\delta_r v$ for $r = 2^m 3^n \delta x, m, n = 0, 1, 2, \ldots$, letting the separation vector magnitude go from δx to $384\delta x = \pi$. δx, the distance between two adjacent points in the grid, is the smallest distance possible between two points for a fixed spatial resolution. On the other extreme, to have a one-one mapping between the choice of the pair of grid-points and $\delta_r v$ in our domain which is 2π periodic, the largest separation distance possible is π. Figures 3e and 3f show the PDFs of $\delta_r v$ for the smallest and largest separation distances for the R_1 and R_4 flow respectively.

Two-dimensional turbulent flows generated by 2DV lack intermittency and as a result, the velocity structure-function PDFs with different separation distances overlap (Boffetta & Ecke, 2012; Boffetta et al., 2000; Dubos et al., 2001; L. M. Smith & Yakhot, 1993, 1994; Sofiadis et al., 2022). These studies point out that in 2D flow devoid of large-scale coherent structures, the PDFs further tend to be Gaussian. However, in 2DV flows with domain-scale coherent vortices, the PDFs can depart from Gaussian, although they still overlap for different separation distances (Boffetta & Ecke, 2012; Boffetta et al., 2000; Dubos et al., 2001; L. M. Smith & Yakhot, 1993, 1994). We see this being the case for the PDFs corresponding to the R_1 flow shown in Figure 3e: the PDFs with grid scale separation distance (red curve) and domain-scale separation distance (blue curve) overlap, although they do not overlap with the Gaussian denoted with the dashed line. A figure similar to this can be seen in Dubos et al. (2001): see Figures 5a and 5b there. In contrast, the R_4 flow's PDFs in Figure 3f shows a different behavior. Notice that for grid scale separation distance (red curve), we see a fat-tailed distribution, while for the domain-scale separation, we see a distribution that overlaps with a Gaussian (blue curve). The PDFs for different

separation distances change and do not overlap with each other, singaling spatial intermittency that is typically observed in three dimensional turbulent flows. Similar PDFs of the structure-functions of two-point velocity statistics moving toward Gaussian with increasing separation distances, is seen in three-dimensional homogeneous isotropic turbulence (Ishihara et al., 2009), see Figure 23 in Laval et al. (2001) and Figures 15 and 16 in Gotoh et al. (2002). This analysis of PDFs reveal that S-2DV can generate flows that transition from typical two-dimensional flows that lack intermittency to those that are characterized by intermittency, as we increase the relative strength of the externally prescribed vorticity field via R.

3.1. Introducing Cyclone-Anticyclone Asymmetry

As seen from Figures 2 and 3, and discussions above, introducing a random external vorticity field in 2DV can help in generating turbulent flows that are intermittent in nature and are not dominated by large scale coherent vortices, along with higher forward energy flux and small-scale energy dissipation. Additionally, these features become more prominent in the flow with increasing strength of the external field, leading to more and more departure from 2DV dynamics.

In addition to the features mentioned above, a key feature often observed in oceanic submesoscale flows is the dominance of cyclonic vorticity structures over anticyclonic ones. This feature is consistently seen in in situ observations, ocean model outputs, and flows generated by idealized models (Brannigan et al., 2015; Buckingham et al., 2016; D'addezio et al., 2020; Rudnick, 2001; Shcherbina et al., 2013; Siegelman, 2020; Thomas & Vishnu, 2022). Such a cyclone-anticyclone asymmetry is not captured by Equation 3; this model disrupts and erodes both cyclonic and anticyclonic vorticity structures with no preferential bias.

To incorporate cyclone-anticyclone asymmetry in the model, we once again draw inspiration from the higher-order slow balanced equation given in Equation 2. As mentioned there, quadratic nonlinear balance-balance interaction terms, denoted with subscript "GG," appear as correction terms at higher orders. Past studies have shown that incorporation of such terms can lead to asymmetric vorticity structures. These terms are quadratic nonlinear terms involving the product of terms such as Q, ∇Q, ψ, $\nabla \psi$, etc. To test the effect of these terms, we temporarily drop the random field and rewrite 2DV as

$$\frac{\partial Q}{\partial t} + \partial[\psi, Q + \epsilon F] = 0, \quad Q = \Delta \psi \tag{11}$$

where F is the quadratic nonlinear term constructed out of different pairwise combinations of the terms Q, ∇Q, ψ, $\nabla \psi$ and $\epsilon \ll 1$ sets the strength of the quadratic term relative to the leading order term, Q. We systematically experimented with terms such as $\psi Q, \psi^2, (\nabla \psi)^2, (\nabla Q)^2, Q^2, \nabla \psi . \nabla Q$, and $\partial[\psi_x, \psi_y]$ and a summary of the effect of including some of these terms is presented in Text S4 in Supporting Information S1. Based on extensive numerical experiments where we monitored the physical space structures and the skewness of the vorticity fields generated, we found that choosing $F = Q^2$ led to flows that consistently and unambiguously favored cyclonic coherent vortices over anticyclonic ones. Finally, we reintroduced the external random field into Equation 11 to get the modified form of S-2DV as

$$\frac{\partial Q}{\partial t} + \partial[\psi, Q + Q_s + \epsilon Q^2] = 0, \quad Q = \Delta \psi \tag{12}$$

As for Equation 3, the above model conserves energy but does not conserve enstrophy. Additionally, while Equation 3 materially conserves $Q + Q_s$, Equation 12 does not have material conservation of $Q + Q_s + \epsilon Q^2$. The advantages of modifying the previous reduced model to construct Equation 12 are shown in Figure 4. Figure 4a shows the vorticity field from integrating Equation 12 with neither the external field nor the asymmetry term, which is essentially 2DV. We see domain-scale coherent vortices with no preference for cyclones or anticyclones. The normalized histogram for this case, with $R = \epsilon = 0$, is shown by the black curve in Figure 4d: note the symmetric distribution of the histogram. Next, Figure 4b shows the vorticity field obtained from integrating Equation 12 with no external field, but retaining the asymmetry term with $\epsilon = 0.25$. We now see that the vorticity is dominated by cyclonic coherent vortices in a background of weak anticyclonic vorticity field. The blue asymmetric histogram in Figure 4d corresponds to this regime and shows that positive vorticity has a fatter tail than negative vorticity. For asymptotically small ϵ values, we found that $\epsilon \ll 0.1$ was too weak to impact coherent
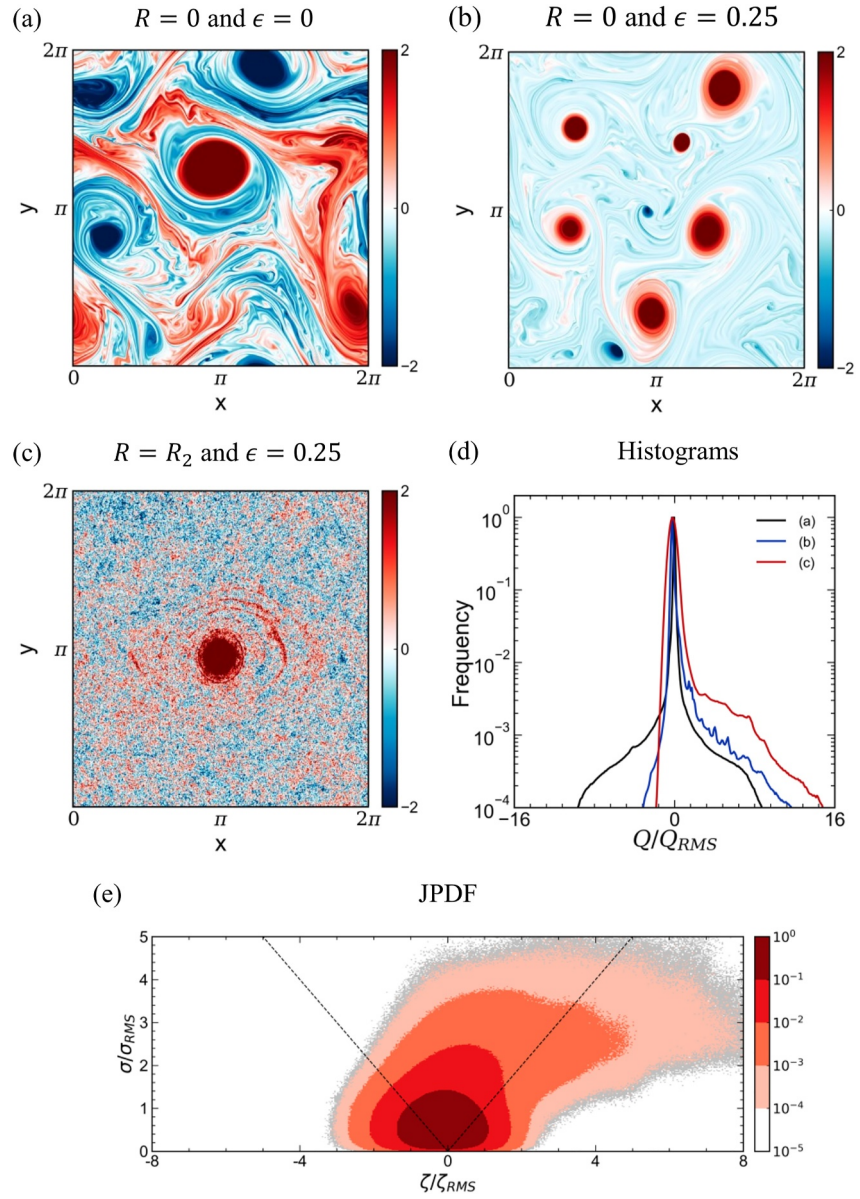
Figure 4. Panels (a), (b), and (c) show the normalized vorticity fields obtained by integrating the model as in Equation 12 with (a) $\epsilon = 0$, $R = 0$, (b) $\epsilon = 0.25$, $R = 0$, and (c) $\epsilon = 0.25$, $R = R_2$. Panel (d) shows the histograms of the normalized vorticity fields corresponding to the flow regimes shown in the panels (a), (b), and (c). Panel (e) shows joint probability density function corresponding to the flow regime shown in panel (c) in strain-vorticity coordinates. Lines with slopes ±1 are drawn with broken lines in this panel.

vortices while $\mathcal{O}(1)$ ϵ values would mean that the Q^2 term in Equation 12 is as strong as the Q term and not a weak perturbation, requiring more stringent time-step constraints for the numerical integrations. In general, we found that $\mathcal{O}(0.1)$ values for ϵ were ideal for generating asymmetric coherent vorticity fields, with cyclonic coherent vortices in an anticyclonic vorticity soup; also see different flows generated in Section 4.

We also examined the skewness of the vorticity fields, that is, the normalized cube of vorticity, as a function of spatial scale and found that the skewness increased as we moved to smaller scales, indicating that the asymmetry in vortex structures continues from large scales where the coherent vortices dominate to small scales. An illustration of this for the flow shown in Figure 4b is given in Figure S5 in Supporting Information S1.
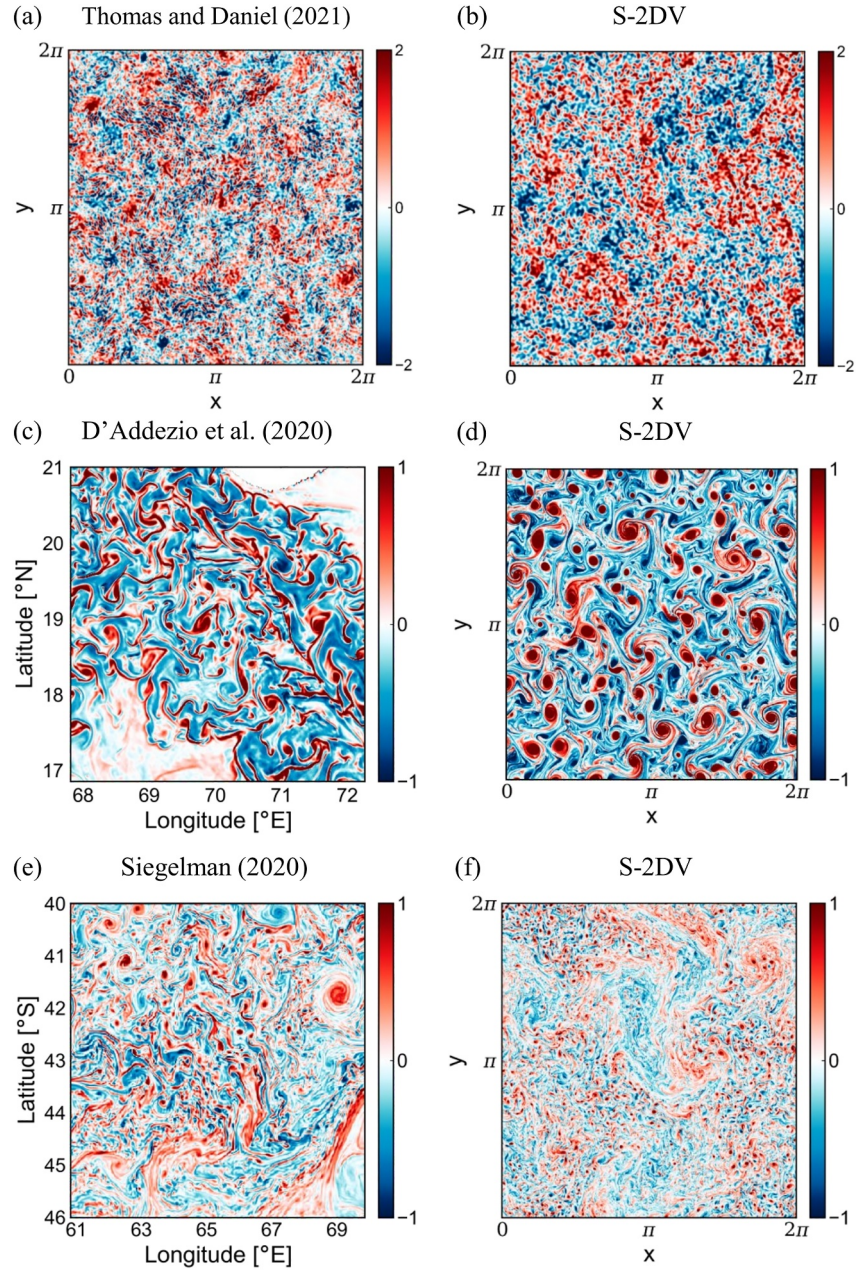
Figure 5. The left column shows the vorticity field from other studies while the right column shows qualitatively matching flows generated by S-2DV. Panel (a) is from a flow regime discussed in Thomas and Daniel (2021), panel (c) is adapted with permission from D'Addezio et al. (2020); copyright 2020 American Meteorological Society, and panel (e) is adapted with permission from Siegelman (2020); copyright 2020 American Meteorological Society.

Figure 4c shows the effect of retaining both the asymmetry term with $\epsilon = 0.25$ and the external field with $R = R_2$. We now see a dominant cyclonic coherent vortex in a soup of broken vorticity structures that largely contains anticyclonic vortices. The red asymmetric histogram in Figure 4d corresponds to this case and shows that positive vorticity has a fatter tail than negative vorticity. To further examine the flow regime highlighted in Figure 4c, we computed the joint probability density function (JPDF) of the flow in strain-vorticity coordinates (Shcherbina et al., 2013) and this is shown in Figure 4e. For this, the normal strain rate and the shear strain rate were computed as $\sigma_n = \partial u/\partial x - \partial v/\partial y$ and $\sigma_s = \partial v/\partial x + \partial u/\partial y$ respectively. These components were then used to find the total strain rate $\sigma = \sqrt{\sigma_n^2 + \sigma_s^2}$.

JPDFs from previous studies show quite a bit of variability, though submesoscale flows with cyclonic structures dominating over anticyclonic ones exhibit higher density along the $\zeta = \sigma$ line (Balwada et al., 2021; Berta et al., 2020; Rocha, Gille, et al., 2016; Xiao et al., 2023). In the JPDF shown in Figure 4e, corresponding to the specific regime highlighted in Figure 4c with a large cyclone floating in a soup which contains anticyclonic vortices, notice the long tail along the line $\zeta/\zeta_{RMS} = \sigma/\sigma_{RMS}$. The higher concentration spread in the direction of this line and less concentration along the line $\zeta/\zeta_{RMS} = -\sigma/\sigma_{RMS}$ is a reflection of the asymmetric vorticity structures, with the cyclonic vorticity dominating over anticyclonic ones.

Overall, the discussion above points out that S-2DV in the form given in Equation 12 is a reduced single-equation model that can generate flows that are rich with small-scale vorticity structures that are skewed toward positive values.

4. Comparison With Some Realistic Submesoscale Flows

In this section, we compare the flows generated by S-2DV with some realistic submesoscale flows generated by complex flow models. We selected flows from several previous studies and integrated the S-2DV model by varying the strength of the external vorticity field, R, and the asymmetry term, ϵ, to generate flows that closely resemble those seen in previous studies.

First, we make a comparison with flows generated by the Boussinesq equations. Figure 5a shows a geostrophic vorticity field obtained by the numerical integration of the three-dimensional non-hydrostatic Boussinesq equation in a regime composed of high-energy waves and low balanced energy. This regime was explored in detail by Thomas and Daniel (2021), and the small-scale features seen in Figure 5a are a result of wave-balance energy exchanges that lead to a forward flux of balanced energy. Notice that the flow does not seem to have cyclone-anticyclone asymmetry; vortical structures of both signs are broken down to small-scale features. To generate similar flows with S-2DV, we experimented with a strong external random vorticity field and no asymmetry term. An example flow obtained with $R = 1.38$ and $\epsilon = 0$ is shown in Figure 5b. Qualitatively, we see similar features in both flows, characterized by broken vorticity structures throughout the domain, with no preference for cyclonic structures over anticyclonic structures.

Next, we make a comparison with submesoscale flows studied by D'addezio et al. (2020) in the Arabian Sea region. The flow was generated by the Navy Coastal Ocean Model that integrates the Boussinesq equations with hydrostatic balance. A vorticity snapshot from this study is shown in Figure 5c, based on the data set discussed in D'addezio et al. (2020). We see prominence of cyclonic coherent vortices in an anticyclonic soup, although no broken fine-scale structures are visible. To replicate this, we experimented with S-2DV in regimes with a weak external random vorticity field but a strong asymmetry term. Based on different tests, Figure 5d shows a flow field generated using $R = 1.47 \times 10^{-3}$ and $\epsilon = 0.25$. The flow generated by S-2DV qualitatively resembles the flow from D'addezio et al. (2020), where cyclonic coherent vortices float in an anticyclonic vorticity soup.

Flows generated by the MIT GCM at $1/48°$resolution were analyzed by Siegelman (2020), and Figure 5e shows the vorticity field in the Antarctic Circumpolar Current region (see Figure 10 there). This flow is again composed of dominant cyclonic vortices in an anticyclonic soup, albeit with some noticeable small-scale anticyclonic vortices. Additionally, in comparison to the flow seen in Figure 5c from D'addezio et al. (2020), we see a lot more fine-scale vorticity structures in Figure 5e. To generate similar flows with S-2DV, we started with parameters that generated flows similar to that shown in Figure 5d, and then experimented with multiple different numerical integrations by gradually increasing the strength of the external random field and decreasing the strength of the asymmetry term. A flow structure resembling Figure 5e is shown in Figure 5f, generated with a numerical integration that used $R = 1.34 \times 10^{-2}$ and $\epsilon = 0.15$.

Solodoch et al. (2023) studied the East Mediterranean Sea circulation using high-resolution numerical simulation outputs from the CROCO model and a snapshot of the vorticity field from their study is given in Figure 6a. Again, we see cyclonic coherent vortices in an anticyclonic vorticity soup and to generate this sort of a flow field, we experimented with parameters close to those used to generate Figure 5d. From the resulting flows we generated, Figure 6b shows a vorticity field corresponding to $R = 1.52 \times 10^{-3}$ and $\epsilon = 0.1$, which qualitatively matches the flow seen in Figure 6a.
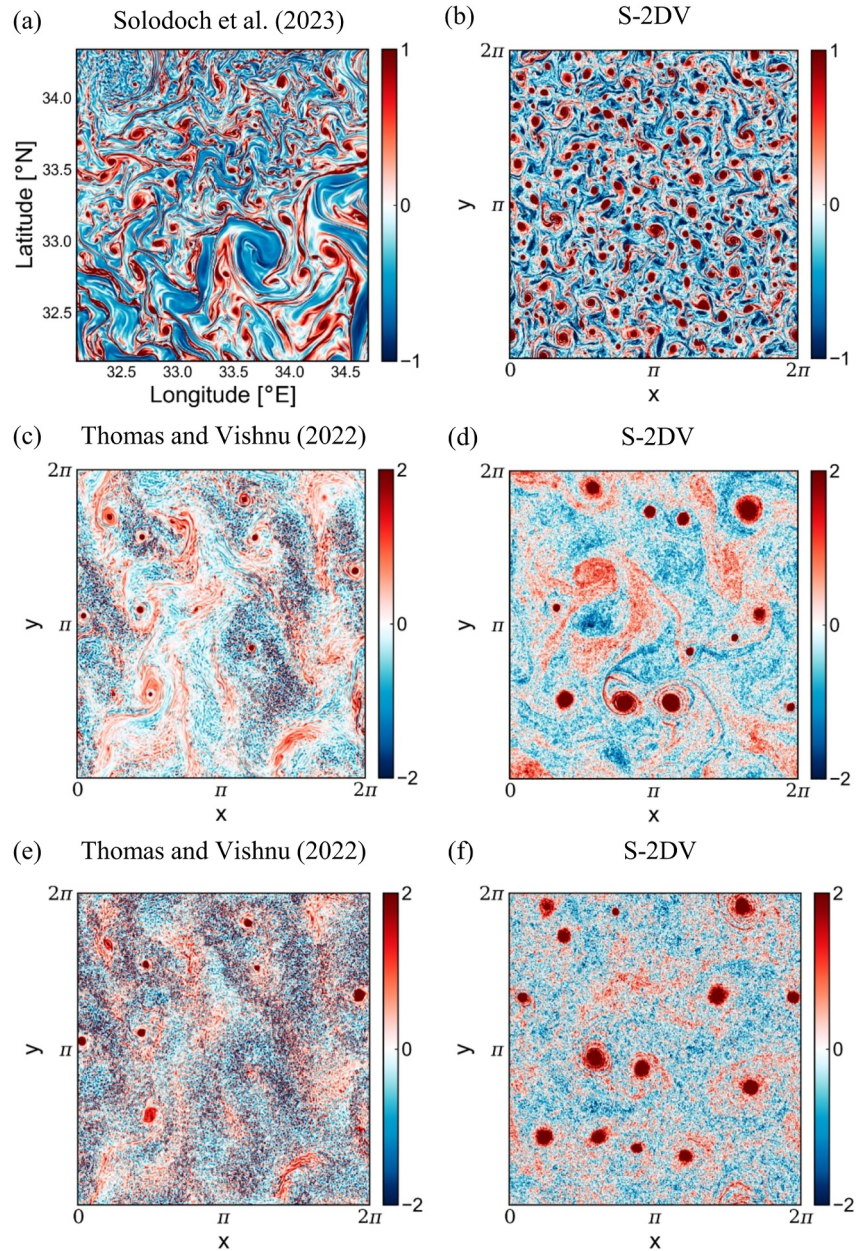
Figure 6. Similar comparison as that shown in Figure 5. Panel (a) is adapted with permission from results discussed in Solodoch et al. (2023); copyright 2023 American Meteorological Society. Panels (c) and (e) correspond to flow regimes discussed in Thomas and Vishnu (2022). Right column shows flow fields generated by S-2DV.

Finally, we compare S-2DV flows with $\mathcal{O}(1)$ Rossby number flows generated by the two-vertical-mode model studied by Thomas and Vishnu (2022), where the Rossby number (Ro) is a parameter in the model. We generated flows with $Ro = 0.5$ and $Ro = 1$, which are shown in Figures 6c and 6e. These flows contain a background of highly energetic small-scale structures and cyclonic coherent vortices in an anticyclonic vorticity soup. To generate similar flows with S-2DV, we had to use a relatively stronger external vorticity field than previous cases and a high asymmetry parameter. Based on a broad set of experiments, Figures 6d and 6f show the flows generated by S-2DV for $\epsilon = 0.25$ and $R = 6.3 \times 10^{-2}$ and $\epsilon = 0.25$ and $R = 0.15$ respectively. We see that S-2DV flows have cyclonic coherent vortices floating in a background soup of broken positive and negative vorticity fragments. While the background soup of vorticity fragments in S-2DV flows matches well with those in
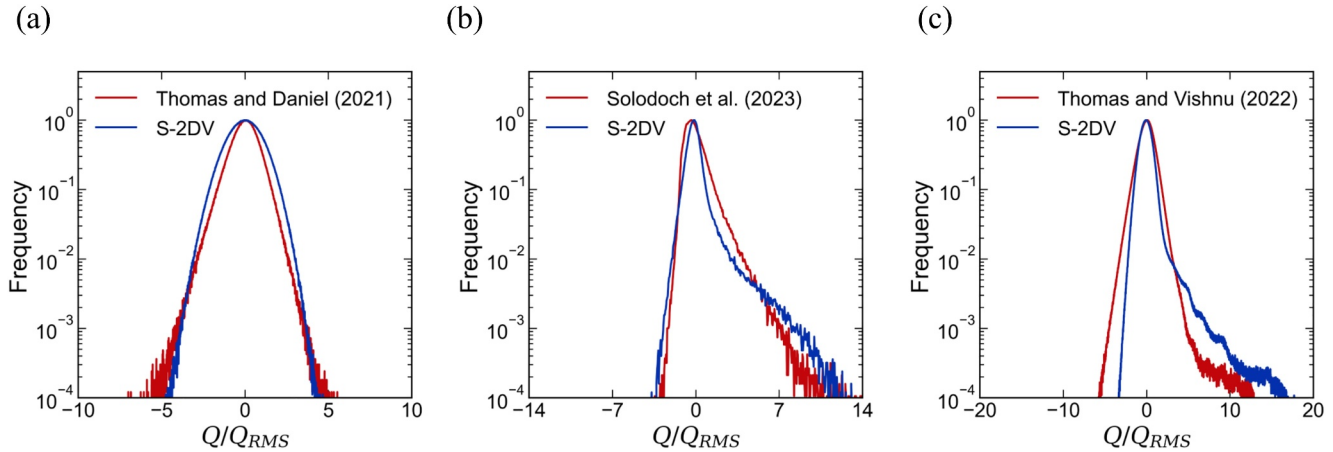
(a)   (b)   (c)

Figure 7. Histograms of normalized vorticity fields corresponding to the physical structures shown in Figures 5 and 6.

the flows generated by the two-vertical-mode model, we see that the cyclonic coherent vortices are larger in size in the S-2DV flows when compared to the two-vertical-mode model flows.

In addition to the physical structures, we also compared the histograms of the flow fields generated by the complex models described above with the S-2DV flows. Three representative comparisons are shown in Figure 7. We collected the vorticity fields over a long interval of time, such that the flow structures shown in the previous figures corresponded to the midpoint of the time interval. To generate the histograms, we normalized the vorticity fields in this time interval for each case by their respective standard deviations. The histograms were further normalized by their maximum frequency for a comparison between the different models, these being the results presented in Figure 7. Further, we used the Wasserstein distance (Villani, 2009) to quantify the comparison between the distributions. The Wasserstein distance, W_d, for two variables ζ_1 and ζ_2 is defined as

$$W_d(\zeta_1, \zeta_2) = \sum_{i=1}^{n} \left| \sum_{j=1}^{i} [P_j(\zeta_1) - P_j(\zeta_2)] \right| \delta(\zeta_1, \zeta_2) \tag{13}$$

where $P_j(\zeta_k)$ is the probability density of ζ_k in the jth interval in the range of ζ_k for $k = 1$ or 2 and the distributions of ζ_1 and ζ_2 have been chunked up into n intervals of the length $\delta(\zeta_1, \zeta_2)$ to compute the PDFs.

To build some intuition about the Wasserstein distance, let us think of the PDF of the first distribution as a mass of soil heaped up in a particular shape. We are tasked with collecting all the material from the first distribution and depositing them in the second in the shape of its PDF. The work done in the process is called the Wasserstein distance or the earth mover's distance (Panaretos & Zemel, 2019; Rubner et al., 2000; Vallender, 1974). Wasserstein distance has been used in optimal transport problems in data visualization, fluid dynamics, and related fields (Benamou & Brenier, 2000; Crook et al., 2024; Ni et al., 2009). When comparing distributions, Wasserstein distance could be as low as 0 for a perfect match between the distributions while it could be really high, with no upper bound, for distributions that have no match. As a result, we expect low values for the Wasserstein distance, preferably less than 1, for distributions that are close to each other.

Figure 7a shows the histogram of vorticity for the flows, similar to that in Figure 5a generated using the Boussinesq equations, and corresponding flows generated using S-2DV, similar to that shown in Figure 5b. Both the distributions are nearly symmetric. The Wasserstein distance between the two distributions was seen to be 0.075, a low value that reflects the degree of agreement between the two distributions. As a second comparison, Figure 7b shows the histograms of the flows from Solodoch et al. (2023) and S-2DV, corresponding to the physical structures in the first row of Figure 6. Notice that both the distributions are asymmetric and skewed. Further, in the positive vorticity regime, the S-2DV distribution falls below that of Solodoch et al. (2023) at low vorticity values while the opposite is seen at high vorticity values. The Wasserstein distance between these distributions was found to be 0.184, this number quantitatively suggesting reasonable similarity between them.

Finally, Figure 7c compares the distributions from $Ro = 1$ flow field generated in Thomas and Vishnu (2022) and S-2DV flow, that is, data corresponding to the sample flow structure comparisons shown in the last row of Figure 6. Although the overall shapes of the two distributions are similar, we see that S-2DV distribution is slightly shifted to the right compared to the distribution from Thomas and Vishnu (2022). As a result, the S-2DV distribution indicates higher positive vorticity values and lower negative vorticity values when compared to that of Thomas and Vishnu (2022). The Wasserstein distance between the two distributions was found to be 0.191, this low value being a reflection of the overall match between the two distributions, despite the shift in mean that is seen in Figure 7c.

Drawing from our efforts to generate the aforementioned flows for comparison with realistic scenarios, we offer insights on how to fine-tune the S-2DV model to produce different flow patterns. Recall that the effect of the external vorticity field is to break down coherent structures to small-scale vortices. More energetic external fields can break down stronger coherent structures, as we saw the traces of the coherent structures diminishing moving from R_1 to R_4 flow in Figure 2. On the other hand, the asymmetry term tends to destroy negative vortices and preserve positive vortices by coalescing them to form cyclonic coherent structures, as we saw in Figure 4 with varying ϵ. The combination of R and ϵ needs to be varied to generate flows with different features. For wave-dominant flows with extremely small-scale structures we needed $R \sim O(1)$ with negligible ϵ, as is seen in the example shown in the first row of Figure 5. For flows containing asymmetric coherent structures, with cyclones dominating, we found that it was better to start with $R \sim O(0.01)$, $\epsilon \sim O(0.1)$. If the flow desired has more smaller scale structures than the flows generated with $R \sim O(0.01)$, it is useful to increase R toward $O(0.1)$. Alternatively, if the flow generated with $R \sim O(0.01)$ had more small-scale features than desired, it is better to decrease R toward $O(0.001)$. Likewise, if the flow desired has fewer larger cyclones than that generated with $\epsilon \sim O(0.1)$, it is useful to increase ϵ, and vice versa. In general we found that the parameter regime $R \sim O(0.001) - O(1)$ and $\epsilon \sim O(0.1)$ could generate relevant realistic flows, as shown in Figures 5 and 6.

We conclude this section with a final remark regarding the comparisons above. As described earlier, the flows from Boussinesq equations seen above are generated in much more complex settings than S-2DV. For instance, Figure 5c from D'addezio et al. (2020) was generated from an ocean model with realistic boundaries that covers a large domain, as indicated by the latitude and longitude labels written on the figure. On the other hand, we integrated S-2DV in an idealized periodic domain $[0, 2\pi]^2$ to generate Figure 5d to compare with Figure 5c. The same holds for the comparisons made in the third row of Figure 5 and the first row of Figure 6. Given these contrasting settings, it might seem unfair to compare such flows. Nevertheless, it is appreciable that a single-equation model like S-2DV can generate flows that qualitatively match features of complex submesoscale flows from realistic models. While a precise one-to-one pointwise match between the flows may not be realized, this ability of the S-2DV model makes it a worthwhile candidate for generating submesoscale-like flows resembling realistic submesoscale flows with limited computational resources. In the following section, we will explore the utility of using the S-2DV model for tracer dispersion applications.

5. Dispersion of Tracers by S-2DV Flows

Given that the S-2DV model can generate mesoscale and submesoscale flow features, as seen above, we now explore the utility of the model for two specific applications involving tracers. In this section, for simplicity, we omit the asymmetry term and examine S-2DV in the presence of the external random vorticity field alone.

5.1. Passive Tracer Dispersion

Passive tracer dispersion in the ocean, and the associated tracer diffusivity, plays a crucial role in accurate climate-scale model predictions (Busecke & Abernathey, 2019; Chouksey et al., 2022; Gnanadesikan et al., 2015; Ragen et al., 2020). Consequently, understanding passive tracer dispersion is important for developing and implementing better parametrizations in large-scale models. Unfortunately, this is a complex problem since the dispersion of passive tracers depends on the details of the flow, and as discussed earlier, the flow dynamics changes with scale. Mesoscale flows are significantly different from submesoscale flows. Therefore, passive tracer dynamics are also different at mesoscales and submesoscales.

Oceanic observations using dye tracers and those examining spice, a passive tracer generated by the linear combination of temperature and salinity, have found signatures of enhanced stirring at submesoscales.
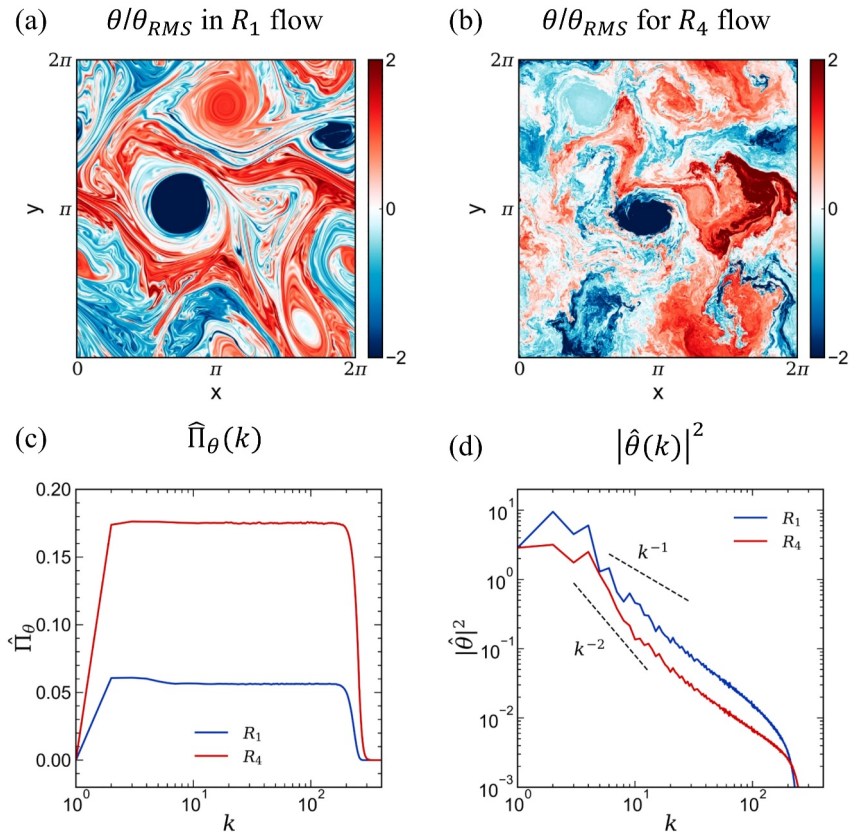
Figure 8. Top panels show the physical structure of the tracer fields normalized by their RMS values for (a) R_1 flow and (b) R_4 flow. Bottom panels show (c) tracer spectral flux and (d) tracer variance spectra for the R_1 and R_4 flow. In panel (d) slope lines k^{-1} and k^{-2} are included for reference.

Diffusivities computed by examining the stretching rate of dye tracers in the ocean have often found significantly higher diffusivities at submesoscales than the estimates predicted based on mesoscale turbulence calculations (Kunze et al., 2015; Polzin & Ferrari, 2004; Shcherbina et al., 2015; Sundermeyer et al., 2020). Furthermore, observations of spice have indicated steeper spectra at submesoscales in comparison to the spectra predicted by mesoscale turbulence theories that are based on quasi-geostrophy (Balwada et al., 2024; Cole & Rudnick, 2012; Jaeger et al., 2020; Klymak et al., 2015; Samelson & Paulson, 1988). More efficient stirring of tracers by flows will result in higher tracer variance flux, leading to steeper tracer spectra. The steeper spectra of spice found in these studies is therefore evidence of more efficient stirring of spice at submesoscales than that estimated based on geostrophic turbulence theories.

Capturing the above mentioned features of passive tracers in submesoscale flows requires expensive, high-resolution numerical models. Without a detailed understanding of the effect the flow has on tracer dynamics, it is challenging to develop accurate parametrizations for large-scale models. While multiple studies have examined passive tracer dispersion by 2DV and QG models that capture mesoscale dynamics (Holloway & Kristmannsson, 1984; Klein et al., 1998; R. K. Scott, 2006; K. S. Smith & Ferrari, 2009), the lack of a similar reduced model that can capture submesoscale flow dynamics has restricted the diversity of studies that have explored tracer dispersion by submesoscale flows. Here, we use S-2DV to compare passive tracer dispersion features by different flows.

The passive tracer dynamics is governed by the equation

$$\frac{\partial \theta}{\partial t} + \partial[\psi, \theta] = 0 \tag{14}$$

where θ is the passive tracer field that is advected by the flow given by the streamfunction ψ obtained from S-2DV, Equation 3. Similar to the flow forcing scheme detailed previously, we forced and maintained the tracer field in spectral space for modes $k < 2$. Additionally, we included a hyperdissipative term $-\nu\Delta^8\theta$ on the right hand side of Equation 14 with hyperviscosity $\nu = 10^{-38}$ to remove tracer variance reaching grid scales. The setup provided us with forced-dissipative equilibrated tracer fields that were advected by the flows generated by S-2DV.

Based on our exploration of passive tracer dispersion across a broad range of R values in Equation 3, Figure 8 shows a comparison between the R_1 flow, which resembles a mesoscale-eddy-rich-flow, and the R_4 flow, that is composed of energetic small-scale features resembling submesoscale flows. Comparing the top panels of Figure 8, we see that the tracer field is trapped as blobs inside coherent vortices of the R_1 flow, with the tracer field getting stretched into fine filaments in the regions outside coherent vortices. In contrast, the energetic small scale structures in the R_4 flow stirs and disperses the tracer field much more efficiently, as can be seen in Figure 8b. Following a procedure analogous to that used to obtain the equation for energy flux of the flow discussed earlier, we obtain the tracer flux equation as

$$\frac{d}{dt}\sum_{p=k_{max}}^{k}|\hat{\theta}_p|^2 = \hat{\Pi}_\theta(k,t) \tag{15}$$

where the effects of the forcing and dissipation are ignored above. $\hat{\Pi}_\theta$ is the spectral flux of the tracer field and Figure 8c shows the tracer flux for R_1 and R_4 flows. Notice that the flux for R_4 flow is more than three times that of the R_1 flow, indicating that the latter is better at stirring and dispersing the tracer than the former, this being a quantification of the result qualitatively inferred by visually comparing the top row of Figure 8.

The increased flux of the tracer field for the R_4 flow leads to more depletion of the tracer field across the inertial range when compared to the R_1 case. This effect is seen in Figure 8d that shows the tracer variance spectra across scales. Notice how the red spectrum is below the blue spectrum, a reflection of the better stirring and dispersion of the tracer field by the R_4 flow. The difference in spectra is qualitatively similar to the tracer spectra reported from oceanic observations discussed earlier: submesoscales stir tracers more efficiently and deplete their concentration in the inertial range than mesoscale flows. The capability of the S-2DV model to generate such complex flows in two-dimensions is a feature that can be helpful to develop submesoscale tracer parametrizations in idealized settings, without having to rely on more complex, expensive ocean models.

5.2. Plankton Population Dynamics

As a second application of the S-2DV model, we consider the effect of different turbulent flows on planktons. The oceanic plankton community is vital for sustaining marine ecosystems and plays an important role in the biogeochemical cycles of our planet. The population and the spread of the plankton community are impacted by the turbulent flow in the ocean; specifically, mesoscale eddies and submesoscale flows spread, and therefore increase the spatial heterogeneity or patchiness of planktons (d'Ovidio et al., 2010; Guasto et al., 2011; Levy et al., 2018; Mahadevan, 2016; Martin, 2003; McGillicuddy, 2016). The widespread availability of various two-dimensional fluid models, including QG model and its reductions, has led to different studies that have examined plankton dynamics in two-dimensions (Abraham, 1998; Bracco et al., 2000; Neufeld, 2012; Perruche et al., 2011). Such idealized studies are helpful for developing and understanding various kinds of plankton models, especially when a large number of plankton species are involved. Here, we explore the utility of the S-2DV model in setting plankton population configuration in a mesoscale-like and a submesoscale-like flow.

We use an idealized coupled phytoplankton-zooplankton model, in line with those used in Neufeld (2012), Perruche et al. (2011), and Abraham (1998).

$$\frac{\partial P}{\partial t} + \partial[\psi, P] = \beta P(1 - P/C(\boldsymbol{x})) - \gamma PZ \tag{16a}$$

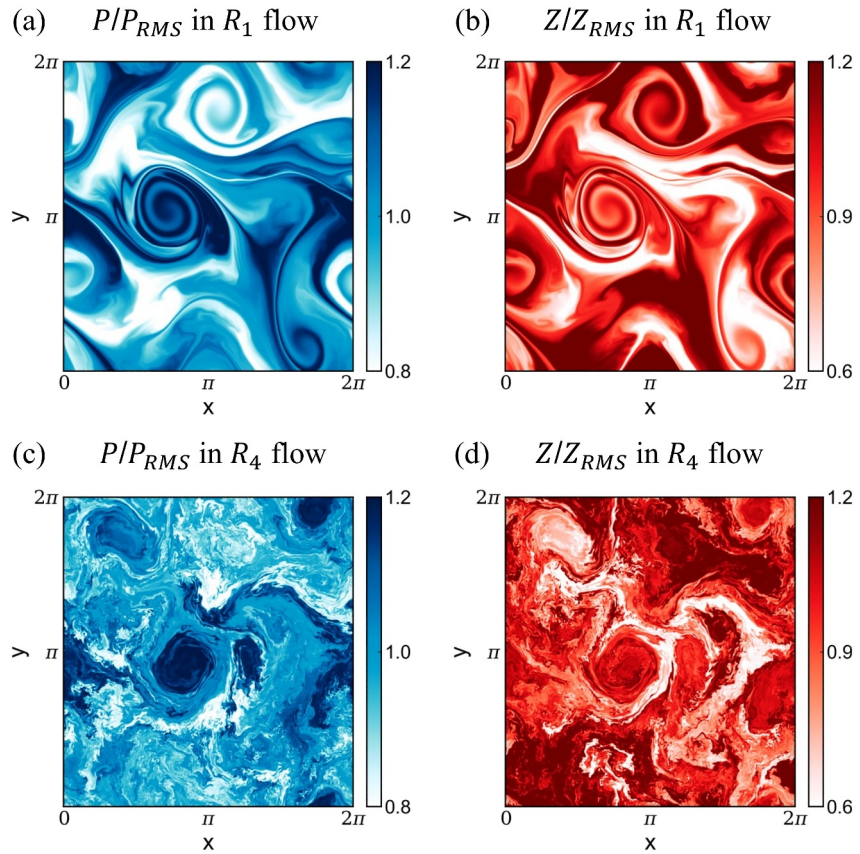$$\frac{\partial Z}{\partial t} + \partial[\psi, Z] = \gamma PZ - \lambda Z \tag{16b}$$

Figure 9. Physical structure of phytoplankton (left column) and zooplankton (right column) normalized by their RMS values for the R_1 flow (top row) and the R_4 flow (bottom row). For easy distinction, blue color map is used for phytoplankton and red color map is used for zooplankton.

In the equations above, P and Z are dynamical variables representing the phytoplankton and zooplankton fields respectively. The phytoplankton equation has a logistic growth and a spatially heterogeneous carrying capacity C, which is the maximum plankton population an element of space can support subject to its constraints depending on the temperature, salinity, exposure to sunlight, abundance of nutrients etc. The term γPZ accounts for the grazing of phytoplankton by zooplankton; this term appears as a sink in 16a and as a source in 16b. The λZ term in 16b represents the zooplankton mortality and serves as a sink in the zooplankton equation. The scalars β, γ and λ determine the balance between different processes in the system, and varying these parameters can help in setting up plankton fields with varying intensity levels.

We numerically integrated Equation 16 in different parameter regimes, and below we will discuss an example comparison of cases. In this example, we set the carrying capacity as $C(\mathbf{x}) = 1 + 0.5 \sin x \sin y$, $\beta = 0.4, \gamma = 0.5, \lambda = 0.2$, and initialized the plankton fields as $P = 4 + \cos x \cos y$ and $Z = 2 + \sin x \sin y$. The growth term, βP, forces the phytoplankton equation while the γPZ term feeds the zooplanktons. Other than these, no external forcing was enforced on the plankton equations. Similar to the passive tracer dynamics discussed in the previous section, we included hyperdissipative terms $-\nu \Delta^8 P$ and $-\nu \Delta^8 Z$ to the phytoplankton and zooplankton equations respectively to remove plankton accumulating at grid scale. However, unlike with passive tracers where we had the hyperviscosity $\nu = 10^{-38}$ equal to that of the flow, we had to set higher values for hyperviscosity, $\nu = 10^{-35}$. This was necessary because the plankton model generated more fine-scale structures due to a stronger cascade of tracer variance to small scales than the passive tracer, requiring more dissipation at the grid scale.

Figure 9 shows the physical structure of the plankton fields based on advecting them with the R_1 flow (top row) and the R_4 flow (bottom row). In the top row, notice the large-scale plankton structures resembling domain-scale flow vortices. In contrast, the bottom row shows much more fine-scale structures as a result of more efficient
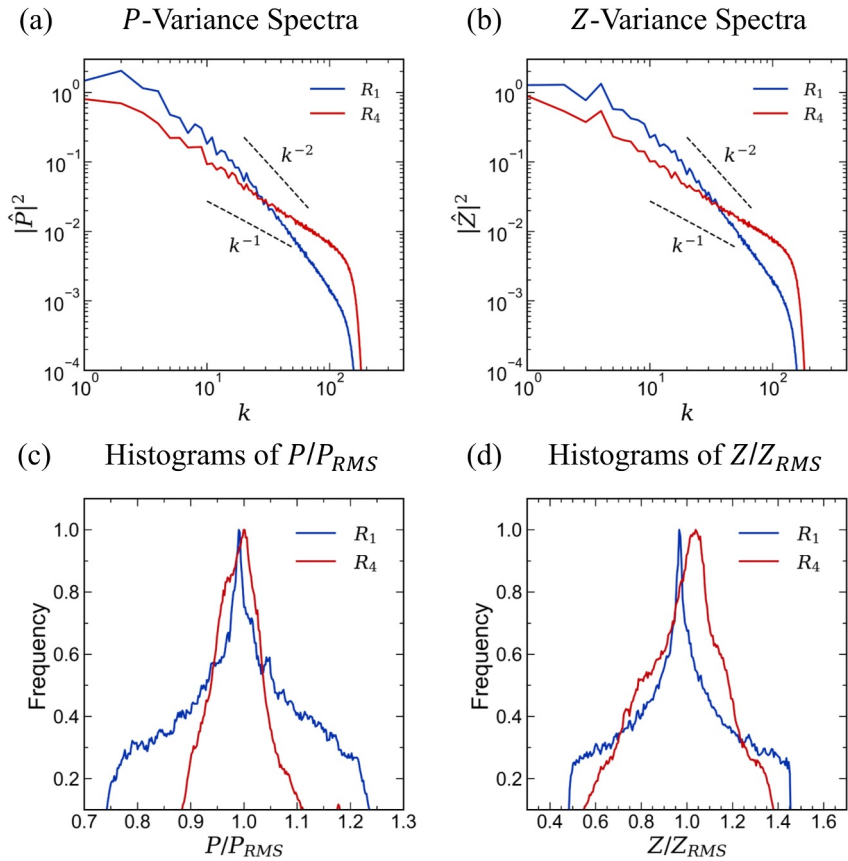
Figure 10. Top row shows (a) phytoplankton and (b) zooplankton spectra for R_1 and R_4 flows. Slope lines k^{-1} and k^{-2} are included in each figure for reference. Bottom row shows the histograms of normalized plankton distribution for (c) phytoplankton and (d) zooplankton.

stirring of the planktons by the R_4 flow. Patchiness is the term that is used to indicate spatial heterogeneity of planktons in the oceans. The presence of finer plankton structures in the bottom row of Figure 9 points out that the R_4 flow is capable of sustaining a higher level of patchiness for the planktons than the R_1 flow. This is further confirmed by an examination of the plankton variance spectra given in the first row of Figure 10. Observe that both phytoplankton (panel a) and zooplankton (panel b) have shallower spectra for the R_4 flow, with more plankton variance at small scales, when compared to the R_1 flow. The R_4 flow due to its energetic small-scale structures is therefore able to maintain a higher level of plankton concentration at smaller scales than the R_1 flow, increasing the patchiness of planktons across scales. Finally, the bottom row of Figure 10 shows the normalized histograms of plankton distributions for the two flows. Notice that the planktons have fatter tails with respect to the RMS values for the R_1 flow, while the histograms for the R_4 shows less spread across the RMS. This is an indication that stirring and homogenization of the plankton distribution are stronger for the R_4 flow than the R_1 flow, leading to lesser spread of the histograms with respect to the RMS for the former than the latter.

The above results illustrate that the S-2DV model can generate turbulent flows capable of maintaining diverse distributions of planktons. In the example we used a simple model composed of just two species, while a realistic model will have several orders of magnitudes of interacting species. This makes it difficult to develop relevant and useful models of planktons. Furthermore, oceanic models are complex and expensive and therefore testing complex dynamical models of interacting planktons in mesoscale-rich and submesoscale-rich flows is a nontrivial challenge. These challenges help us appreciate the utility of S-2DV, which can serve as the first test bed for development and implementation of plankton and related biogeochemical models with modest resources.

6. Summary and Discussion

Oceanic mesoscale dynamics are well-captured by the QG equation and its variants; this reduced model generating flows with large-scale coherent vortices as a result of the inverse cascade of the flow energy. The simplicity and ease of use of this preliminary model have made it enormously popular, leading to its widespread application across a variety of fields. Contrary to mesoscale flows, submesoscale flows in the ocean are composed of energetic small-scale flow structures, cyclone-anticyclone asymmetry, forward energy flux, and enhanced small-scale dissipation; these features being outside the scope of flows generated by balanced reduced models like QG. The present work was aimed at developing a reduced two-dimensional model, starting from the barotropic QG or the two-dimensional vorticity (2DV) equation, capable of generating flows with submesoscale-like features mentioned above.

In pursuit of developing a reduced equation, we drew inspiration from higher-order balanced asymptotic models that incorporate nonlinear balance-balance and wave-wave interaction terms. Based on this insight, we added an external vorticity field in the Jacobian of the 2DV equation, such that the new model conserves flow energy but does not conserve flow enstrophy. The lack of the dual conservation of energy and enstrophy prevents an inverse energy cascade in the new model, which we termed the submesoscale two-dimensional vorticity (S-2DV) equation. For weak external fields, the flows generated are identical to those generated by 2DV. However, on increasing strength of the external field, S-2DV flows were seen to undergo a transition from mesoscale-like flow, consisting of domain-scale coherent vortices with an inverse energy flux, to submesoscale-like flows, composed of a forward energy flux with broken vorticity structures scattered throughout the domain. Furthermore, S-2DV flows were characterized by intermittency, a feature observed in complex three-dimensional turbulent flows but absent in two-dimensional flows generated by the 2DV model.

Once again taking inspiration from the nonlinear balance-balance terms in higher-order balanced models, we expanded the new reduced model by incorporating the preference for asymmetric vorticity fields. Oceanic flows at submesoscales are characterized by cyclonic vortices dominating over anticyclonic vortices. By systematic experimentation with different terms, we found that the introduction of an additional vorticity-squared term in the S-2DV equation could generate flow fields that favored cyclonic vortices over anticyclonic vortices. Finally, changing the strength of the external random vorticity field and the asymmetry term was seen to generate submesoscale-like flows where coherent cyclonic vortices floated in a background soup of broken anticyclonic vorticity structures.

Although insights from asymptotic models and turbulent flow dynamics in different settings inspired the construction of the S-2DV model in the form discussed in this work, this reduced model is not one that can be derived from first principles. Consequently, the model is an ad hoc one, that is, one that is artificially constructed based on intuition. In the introduction, we discussed kinematic flow models, that are similarly not derived but constructed intuitively with the goal of generating turbulent flows with different levels of complexity. We also discussed dynamic models like surface QG and semi-geostrophic models that can be derived systematically. In terms of its derivation and mathematical rigor, the reduced model we describe in this work may be considered somewhere in between the ad hoc kinematic models and the various kinds of dynamic models that can be systematically derived. We developed our model building up on a higher-order asymptotic model, requiring physical principles such as energy conservation, and based on physical insights gained from numerical experiments.

Despite the ad hoc nature of the model, a single-equation model generating intricate flows resembling those from much more complex models is a nontrivial achievement. To test the capability of the model in this direction, we compared flows generated by S-2DV with the vorticity fields generated by complex submesoscale-rich flows generated by the Boussinesq equations in different oceanographic regions and at different Rossby numbers. The flow structures and histograms of the vorticity fields from these complex models were seen to reasonably match those of S-2DV. The results of the comparisons reveal that S-2DV can serve as a useful model that is capable of generating submesoscale-like flow features, while not explicitly modeling many complex agents such as internal gravity waves and other ageostrophic modes that are responsible for such dynamics.

Having gotten a handle on the features of S-2DV, we used the flows it generated for two applications. The first one was passive tracer dispersion in the ocean. Multiple oceanic observations in the past have indicated enhanced stirring and dispersion of passive tracers at submesoscales when compared to mesoscales. This feature was seen to be captured by advecting a passive tracer field using S-2DV flows with external fields of different strengths.

Tracer flux and dispersion was much higher for submesoscale-like flows generated by S-2DV, in agreement with the oceanic observations noted above. The second application was connected to the patchiness of planktons in the ocean. Plankton species exhibit a high level of spatial heterogeneity, identified as patchiness, which is crucial for the coexistence of a large number of plankton species with limited resources. Using S-2DV to generate mesoscale-like and submesoscale-like flows and advecting plankton species with the flows, we found that a higher level of patchiness could be maintained by the submesoscale-like flow.

The applications discussed above are two examples where a reduced model that generates submesoscale-like flow is useful. Indeed, it is important to note that the S-2DV model is by no means expected to replace realistic high-resolution, complex, submesoscale flow models. In contrast, the model can serve as a low cost alternative to generate small-scale rich flows for different kinds of applications. Developing tracer parameterizations and plankton ecosystem models that thrive in complex oceanic flows require easy access to models that can generate turbulent flows with desired small-scale features. On the one extreme, QG model and its variants can generate coherent vortex dominated mesoscale-like flows. The results of this study point out that S-2DV can be used as a reduced model to generate two-dimensional flows that encompasses features of submesoscale flows, and can therefore serve as a first test-bed for applications that rely on having access to small-scale rich flows.

We conclude by pointing out some useful extensions of the S-2DV model. To test the effects of introducing unbalanced modes in the simplest balanced model available, we used the barotropic QG or the 2DV equation. If we set $Q = \left(\Delta - 1/L_D^2 \right)\psi$ in Equation 1, the base model becomes the shallow water QG equation with a finite deformation length L_D. As part of this work, we introduced an external random field term in this shallow water QG model and repeated the experiments discussed above for 2DV. Although we did find quantitative changes in the results, the qualitative results such as the forward energy flux, enhanced small-scale dissipation, intermittency, etc were similar for the shallow-water QG model as well. Another advanced extension of the model, that we did not attempt but is not too difficult to implement, is using the external random field in the upper layer of a two-layer shallow water QG model. Since the mixed layer in the ocean is an active zone of submesoscale dynamics, this extension can generate a upper flow region with energetic small-scale features while the lower region can remain as conventional QG flow region. Such a two-layer model with vertical variability can be used for a wider set of applications than the ones we presented in this work. We hope that S-2DV and its extended variants get used for different applications in the future.

Data Availability Statement

The data sets used for the results in this article are available at Gowthaman (2024).

References

Abraham, E. R. (1998). The generation of plankton patchiness by turbulent stirring. *Nature*, *391*(6667), 577–580. https://doi.org/10.1038/35361

Allen, J. S. (1993). Iterated geostrophic intermediate models. *Journal of Physical Oceanography*, *23*(11), 2447–2461. https://doi.org/10.1175/1520-0485(1993)023<2447:igim>2.0.co;2

Balwada, D., Gray, A., Dove, L. A., & Thompson, A. (2024). Tracer stirring and variability in the Antarctic circumpolar current near the southwest Indian ridge. *JGR: Oceans*, *129*(1), e2023JC019811. https://doi.org/10.1029/2023jc019811

Balwada, D., Xiao, Q., Smith, S., Abernathey, R., & Gray, A. R. (2021). Vertical fluxes conditioned on vorticity and strain reveal submesoscale ventilation. *Journal of Physical Oceanography*, *51*, 2883–2901.

Benamou, J., & Brenier, Y. (2000). A computational fluid mechanics solution to the monge-kantorovich mass transfer problem. *Numerische Mathematik*, *84*(3), 375–393. https://doi.org/10.1007/s002110050002

Berta, M., Griffa, A., Haza, A. C., Horstmann, J., Huntley, H. S., Ibrahim, R., et al. (2020). Submesoscale kinematic properties in summer and winter surface flows in the northern Gulf of Mexico. *Journal of Geophysical Research: Oceans*, *125*(10), e2020JC016085. https://doi.org/10.1029/2020jc016085

Boffetta, G., Celani, A., & Vergassola, M. (2000). Inverse energy cascade in two-dimensional turbulence: Deviations from Gaussian behavior. *Physical Review E - Statistical Physics, Plasmas, Fluids, and Related Interdisciplinary Topics*, *61*(1), R29–R32. https://doi.org/10.1103/physreve.61.r29

Boffetta, G., & Ecke, R. E. (2012). Two-dimensional turbulence. *Annual Review of Fluid Mechanics*, *44*(1), 427–451. https://doi.org/10.1146/annurev-fluid-120710-101240

Bracco, A., Provenzale, A., & Scheuring, I. (2000). Mesoscale vortices and the paradox of the plankton. *Proceedings of the Royal Society of London B.*, *267*(1454), 1795–1800. https://doi.org/10.1098/rspb.2000.1212

Brannigan, L., Marshall, D. P., Naveira-Garabato, A., & G, N. A. J. (2015). The seasonal cycle of submesoscale flows. *Ocean Modelling*, *92*, 69–84. https://doi.org/10.1016/j.ocemod.2015.05.002

Buckingham, C. E. e. a., Naveira Garabato, A. C., Thompson, A. F., Brannigan, L., Lazar, A., Marshall, D. P., et al. (2016). Seasonality of submesoscale flows in the ocean surface boundary layer. *Geophysical Research Letters*, *43*(5), 2118–2126. https://doi.org/10.1002/2016gl068009

Busecke, J. J. M., & Abernathey, R. P. (2019). Ocean mesoscale mixing linked to climate variability. *Science Advances*, *5*(1), eaav5014. https://doi.org/10.1126/sciadv.aav5014

Callies, J., Ferrari, R., Klymak, J., & Gula, J. (2015). Seasonality in submesoscale turbulence. *Nature Communications*, *6*(1), 6862. https://doi.org/10.1038/ncomms7862

Cao, H., Jing, Z., Fox-Kemper, B., Yan, T., & Qi, Y. (2019). Scale transition from geostrophic motions to internal waves in the northern south China sea. *Journal of Geophysical Research: Oceans*, *124*(12), 9364–9383. https://doi.org/10.1029/2019jc015575

Capet, X., McWilliams, J. C., Molemaker, M. J., & Shchepetkin, A. F. (2008a). Mesoscale to submesoscale transition in the California current system: Energy balance and flux. *Journal of Physical Oceanography*, *38*(10), 2256–2269. https://doi.org/10.1175/2008jpo3810.1

Capet, X., McWilliams, J. C., Molemaker, M. J., & Shchepetkin, A. F. (2008b). Mesoscale to submesoscale transition in the California current system: Flow structure, eddy flux, and observational tests. *Journal of Physical Oceanography*, *38*(1), 29–43. https://doi.org/10.1175/2007jpo3671.1

Chelton, D. B., Schlax, M. G., & Samelson, R. M. (2011). Global observations of nonlinear mesoscale eddies. *Progress in Oceanography*, *91*(2), 167–216. https://doi.org/10.1016/j.pocean.2011.01.002

Chouksey, A., Griesel, A., Chouksey, M., & Eden, C. (2022). Changes in global ocean circulation due to isopycnal diffusion. *Journal of Physical Oceanography*, *52*(9), 2219–2235. https://doi.org/10.1175/jpo-d-21-0205.1

Cole, S., & Rudnick, D. (2012). The spatial distribution and annual cycle of upper ocean thermohaline structure. *Journal of Geophysical Research*, *117*(C2), C02027. https://doi.org/10.1029/2011jc007033

Crook, O. M., Cucuringu, M., Hurst, T., Schönlieb, C., Thorpe, M., & Zygalakis, K. C. (2024). A linear transportation lp distance for pattern recognition. *Pattern Recognition*, *147*, 110080. https://doi.org/10.1016/j.patcog.2023.110080

D'addezio, J. M., Jacobs, G. A., Yaremchuk, M., & Souopgui, I. (2020). Submesoscale eddy vertical covariances and dynamical constraints from high-resolution numerical simulations. *Journal of Physical Oceanography*, *50*(4), 1087–1115. https://doi.org/10.1175/jpo-d-19-0100.1

Delpech, A., Barkan, R., Srinivasan, K., McWilliams, J., Arbic, B., Siyanbola, O. Q., & Buijsman, M. (2024). Eddy–internal wave interactions and their contribution to cross-scale energy fluxes: A case study in the California current. *Journal of Physical Oceanography*, *54*(3), 741–754. https://doi.org/10.1175/jpo-d-23-0181.1

d'Ovidio, F., De Monte, S., Alvain, S., Dandonneau, Y., & Lévy, M. (2010). Fluid dynamical niches of phytoplankton types. *Proceedings of the National Academy of Sciences of the United States of America*, *107*(43), 18366–18370. https://doi.org/10.1073/pnas.1004620107

Dubos, T., Babiano, A., Paret, J., & Tabeling, P. (2001). Intermittency and coherent structures in the two-dimensional inverse energy cascade: Comparing numerical and laboratory experiments. *Physical Review E - Statistical Physics, Plasmas, Fluids, and Related Interdisciplinary Topics*, *64*(3), 036302. https://doi.org/10.1103/physreve.64.036302

Ferrari, R., & Wunsch, C. (2009). Ocean circulation kinetic energy: Reservoirs, sources and sinks. *Annual Review of Fluid Mechanics*, *41*(1), 253–282. https://doi.org/10.1146/annurev.fluid.40.111406.102139

Gnanadesikan, A., Pradal, M. A., & Abernathey, R. (2015). Isopycnal mixing by mesoscale eddies significantly impacts oceanic anthropogenic carbon uptake. *Geophysical Research Letters*, *42*(11), 4249–4255. https://doi.org/10.1002/2015gl064100

Gotoh, T., Fukayama, D., & Nakano, T. (2002). Velocity field statistics in homogeneous steady turbulence obtained using a high-resolution direct numerical simulation. *Physics of Fluids*, *14*(3), 1065–1081. https://doi.org/10.1063/1.1448296

Gowthaman, K. (2024). GT24 [Dataset]. *Zenodo*. https://doi.org/10.5281/zenodo.11062548

Guasto, J., Rusconi, R., & Stocker, R. (2011). Fluid mechanics of planktonic microorganisms. *Annual Review of Fluid Mechanics*, *44*(1), 373–400. https://doi.org/10.1146/annurev-fluid-120710-101156

Hakim, G., Snyder, C., & Muraki, D. (2002). A new surface model for cyclone-anticyclone asymmetry. *Journal of the Atmospheric Sciences*, *59*(16), 2405–2420. https://doi.org/10.1175/1520-0469(2002)059<2405:ansmfc>2.0.co;2

Hart, J. E. (1979). Barotropic quasi-geostrophic flow over anisotropic mountains. *Journal of the Atmospheric Sciences*, *36*(9), 1736–1746. https://doi.org/10.1175/1520-0469(1979)036<1736:bqgfoa>2.0.co;2

Holloway, G. (1987). Systematic forcing of large-scale geophysical flows by eddy-topography interaction. *Journal of Fluid Mechanics*, *184*, 463–476. https://doi.org/10.1017/s0022112087002970

Holloway, G., & Kristmannsson, S. S. (1984). Stirring and transport of tracer fields by geostrophic turbulence. *Journal of Fluid Mechanics*, *141*, 27–50. https://doi.org/10.1017/s0022112084000720

Hoskins, B. J., & Bretherton, F. (1972). Atmospheric frontogenesis models: Mathematical formulation and solutions. *Journal of the Atmospheric Sciences*, *29*(1), 11–37. https://doi.org/10.1175/1520-0469(1972)029<0011:afmmfa>2.0.co;2

Ishihara, T., Gotoh, T., & Kaneda, Y. (2009). Study of high–Reynolds number isotropic turbulence by direct numerical simulation. *Annual Review of Fluid Mechanics*, *41*(1), 165–180. https://doi.org/10.1146/annurev.fluid.010908.165203

Jaeger, G. S., MacKinnon, J. A., Lucas, A. J., Shroyer, E., Nash, J., Tandon, A., et al. (2020). How spice is stirred in the Bay of Bengal. *Journal of Physical Oceanography*, *50*(9), 2669–2688. https://doi.org/10.1175/jpo-d-19-0077.1

Klein, P., Treguier, A. M., & Hua, B. L. (1998). Three-dimensional stirring of thermohaline fronts. *Journal of Marine Research*, *56*(3), 589–612. https://doi.org/10.1357/002224098765213595

Klymak, J. M., Crawford, W., Alford, M. H., MacKinnon, J. A., & Pinkel, R. (2015). Along-isopycnal variability of spice in the north pacific. *Journal of Geophysical Research: Oceans*, *120*(3), 2287–2307. https://doi.org/10.1002/2013jc009421

Kraichnan, R. (1970). Diffusion by a random velocity field. *Physics of Fluids*, *11*(1), 22–31. https://doi.org/10.1063/1.1692799

Kunze, E., Klymak, J. M., Lien, R. C., Ferrari, R., Lee, M. A., Sundermeyer, C. M., & Goodman, L. (2015). Submesoscale water-mass spectra in the Sargasso Sea. *Journal of Physical Oceanography*, *45*(5), 1325–1338. https://doi.org/10.1175/jpo-d-14-0108.1

Lapeyre, G. (2017). Surface quasi-geostrophy. *Fluids*, *2*(1), 7. https://doi.org/10.3390/fluids2010007

Lapeyre, G., & Klein, P. (2006). Dynamics of the upper oceanic layers in terms of surface quasigeostrophy theory. *Journal of Physical Oceanography*, *32*(2), 165–176. https://doi.org/10.1175/jpo2840.1

Laval, J.-P., Dubrulle, B., & Nazarenko, S. (2001). Nonlocality and intermittency in three-dimensional turbulence. *Physics of Fluids*, *13*(7), 1995–2012. https://doi.org/10.1063/1.1373686

Levy, M., Frank, P. J., & Smith, S. K. (2018). The role of submesoscale currents in structuring marine ecosystems. *Nature Communications*, *9*(1), 4758. https://doi.org/10.1038/s41467-018-07059-3

Li, L., Deremble, B., Lahaye, N., & Mémin, E. (2023). Stochastic data-driven parameterization of unresolved eddy effects in a baroclinic quasi-geostrophic model. *Journal of Advances in Modeling Earth Systems*, *15*(2), e2022MS003297. https://doi.org/10.1029/2022ms003297

Lien, R.-C., & Sanford, T. B. (2019). Small-scale potential vorticity in the upper ocean thermocline. *Journal of Physical Oceanography*, *49*(7), 1845–1872. https://doi.org/10.1175/jpo-d-18-0052.1

Mahadevan, A. (2016). The impact of submesoscale physics on primary productivity of plankton. *Annual Review of Marine Science*, *8*(1), 161–184. https://doi.org/10.1146/annurev-marine-010814-015912

Martin, A. P. (2003). Phytoplankton patchiness: The role of lateral stirring and mixing. *Progress in Oceanography*, *57*(2), 125–174. https://doi.org/10.1016/s0079-6611(03)00085-5

McGillicuddy, D. J. (2016). Mechanisms of physical-biological-biogeochemical interaction at the oceanic mesoscale. *Annual Review of Marine Science*, *8*(1), 125–159. https://doi.org/10.1146/annurev-marine-010814-015606

McWilliams, J. C., & Gent, P. R. (1980). Intermediate models of planetary circulations in the atmosphere and ocean. *Journal of the Atmospheric Sciences*, *37*(8), 1657–1678. https://doi.org/10.1175/1520-0469(1980)037<1657:imopci>2.0.co;2

Meacham, J., & Berloff, P. (2023). On clustering of floating tracers in random velocity fields. *Journal of Advances in Modeling Earth Systems*, *15*(5), e2022MS003484. https://doi.org/10.1029/2022ms003484

Muraki, D., Snyder, C., & Rotunno, R. (1999). The next-order corrections to quasigeostrophic theory. *Journal of the Atmospheric Sciences*, *56*(11), 1547–1560. https://doi.org/10.1175/1520-0469(1999)056<1547:tnoctq>2.0.co;2

Neufeld, Z. (2012). Stirring effects in models of oceanic plankton populations. *Chaos*, *22*(3), 037102. https://doi.org/10.1063/1.4751329

Ni, K., Bresson, X., Chan, T., & Esedoglu, S. (2009). Local histogram based segmentation using the Wasserstein distance. *International Journal of Computer Vision*, *84*(1), 97–111. https://doi.org/10.1007/s11263-009-0234-0

Panaretos, V. M., & Zemel, Y. (2019). Statistical aspects of wasserstein distances. *Annual Review of Statistics and Its Application*, *6*(1), 405–431. https://doi.org/10.1146/annurev-statistics-030718-104938

Perruche, C., Rivière, P., Lapeyre, G., Carton, X., & Pondaven, P. (2011). Effects of surface quasi-geostrophic turbulence on phytoplankton competition and coexistence. *Journal of Marine Research*, *69*(1), 105–135. https://doi.org/10.1357/002224011798147606

Pinkel, R. (2014). Vortical and internal wave shear and strain. *Journal of Physical Oceanography*, *44*(8), 2070–2092. https://doi.org/10.1175/jpo-d-13-090.1

Poje, A. C., Ozgokmen, T. M., Bogucki, D. J., & Kirwan, A. D. (2017). Evidence of a forward energy cascade and Kolmogorov self-similarity in submesoscale ocean surface drifter observations. *Physics of Fluids*, *29*(2), 020701. https://doi.org/10.1063/1.4974331

Polzin, K. L., & Ferrari, R. (2004). Isopycnal dispersion in nature. *Journal of Physical Oceanography*, *34*(1), 247–257. https://doi.org/10.1175/1520-0485(2004)034<0247:idin>2.0.co;2

Qiu, B., Nakano, T., Chen, S., & Klein, P. (2017). Submesoscale transition from geostrophic flows to internal waves in the northwestern pacific upper ocean. *Nature Communications*, *8*(1), 14055. https://doi.org/10.1038/ncomms14055

Qiu, B., Nakano, T., Chen, S., & Klein, P. (2022). Bi-directional energy cascades in the Pacific Ocean from equator to subarctic gyre. *Geophysical Research Letters*, *49*(8), e2022GL097713. https://doi.org/10.1029/2022gl097713

Ragen, S., Pradal, M. A., & Gnanadesikan, A. (2020). The impact of parameterized lateral mixing on the Antarctic circumpolar current in a coupled climate model. *Journal of Physical Oceanography*, *50*(4), 965–982. https://doi.org/10.1175/jpo-d-19-0249.1

Ragone, F., & Badin, G. (2016). A study of surface semi-geostrophic turbulence: Freely decaying dynamics. *Journal of Fluid Mechanics*, *792*, 740–774. https://doi.org/10.1017/jfm.2016.116

Richman, J. G., Arbic, B. K., Shriver, J. F., Metzger, E. J., & Wallcraft, A. J. (2012). Inferring dynamics from the wavenumber spectra of an eddying global ocean model with embedded tides. *Journal of Geophysical Research*, *117*(C12), C12012. https://doi.org/10.1029/2012jc008364

Rocha, C. B., Chereskin, T. K., Gille, S. T., & Menemenlis, D. (2016). Mesoscale to submesoscale wavenumber spectra in drake passage. *Journal of Physical Oceanography*, *46*(2), 601–620. https://doi.org/10.1175/jpo-d-15-0087.1

Rocha, C. B., Gille, S. T., Chereskin, T. K., & Menemenlis, D. (2016). Seasonality of submesoscale dynamics in the Kuroshio extension. *Geophysical Research Letters*, *43*(21), 11304–11311. https://doi.org/10.1002/2016gl071349

Rotunno, R., Muraki, D. M., & Snyder, C. (2000). Unstable baroclinic waves beyond quasi-geostrophic theory. *Journal of the Atmospheric Sciences*, *57*(19), 3285–3295. https://doi.org/10.1175/1520-0469(2000)057<3285:ubwbqt>2.0.co;2

Rubner, Y., Tomasi, C., & Guibas, L. J. (2000). The earth mover's distance as a metric for image retrieval. *International Journal of Computer Vision*, *40*, 99–121.

Rudnick, D. L. (2001). On the skewness of vorticity in the upper ocean. *Geophysical Research Letters*, *28*(10), 2045–2048. https://doi.org/10.1029/2000gl012265

Salmon, R. (1978). *Lectures on geophysical fluid dynamics*. Oxford University Press.

Samelson, R. M., & Paulson, C. A. (1988). Towed thermistor chain observations of fronts in the subtropical north pacific. *Journal of Geophysical Research*, *93*(C3), 2237–2246. https://doi.org/10.1029/jc093ic03p02237

Savage, A. C., Arbic, B. K., Richman, J. G., Shriver, J. F., Alford, M. H., Buijsman, M. C., et al. (2017). Frequency content of sea surface height variability from internal gravity waves to mesoscale eddies. *Journal of Geophysical Research: Oceans*, *122*, 2519–2538. https://doi.org/10.1002/2016JC012331

Scott, R. B., & Wang, F. M. (2005). Direct evidence of an oceanic inverse kinetic energy cascade from satellite altimetry. *Journal of Physical Oceanography*, *35*(9), 1650–1666. https://doi.org/10.1175/jpo2771.1

Scott, R. K. (2006). Local and nonlocal advection of a passive scalar. *Physics of Fluids*, *56*, 122–125.

Shcherbina, A. Y., D'Asaro, E. A., Lee, C., Klymak, J. M., Molemaker, M. J., & McWilliams, J. C. (2013). Statistics of vertical vorticity, divergence, and strain in a developed submesoscale turbulence field. *Geophysical Research Letters*, *40*(17), 4706–4711. https://doi.org/10.1002/grl.50919

Shcherbina, A. Y., Sundermeyer, M. A., Kunze, E., D'Asaro, E., Badin, G., Birch, D., et al (2015). The latmix summer campaign: Submesoscale stirring in the upper ocean. *Bulletin America Meteorology Social*, *96*, 1257–1279.

Siegelman, L. (2020). Energetic submesoscale dynamics in the ocean interior. *Journal of Physical Oceanography*, *50*(3), 727–749. https://doi.org/10.1175/jpo-d-19-0253.1

Siegelman, L., Klein, P., Riviere, P., Thompson, A. F., Torres, H. S., Flexas, M., & Menemenlis, D. (2020). Enhanced upward heat transport at deep submesoscale ocean fronts. *Nature Geoscience*, *13*(1), 50–55. https://doi.org/10.1038/s41561-019-0489-1

Sirohi, M., & Thomas, J. (2024). Passive tracer dispersion by idealized flows across Rossby numbers. *Journal of Physical Oceanography*, *54*(9), 1889–1902. https://doi.org/10.1175/jpo-d-23-0132.1

Smith, K. S., & Ferrari, R. (2009). The production and dissipation of compensated thermohaline variance by mesoscale stirring. *Journal of Physical Oceanography*, *39*(10), 2477–2501. https://doi.org/10.1175/2009jpo4103.1

Smith, L. M., & Yakhot, V. (1993). Bose condensation and small-scale structure generation in a random force driven 2d turbulence. *Physical Review Letters*, *71*(3), 352–355. https://doi.org/10.1103/physrevlett.71.352

Smith, L. M., & Yakhot, V. (1994). Finite-size effects in forced two-dimensional turbulence. *Journal of Fluid Mechanics*, *274*, 115–138. https://doi.org/10.1017/s0022112094002065

Sofiadis, G., Sarris, I. E., & Alexakis, A. E. (2022). Inducing intermittency in the inverse cascade of two-dimensional turbulence by a fractal forcing. *Physical Review Fluids*, *8*(2), 024607. https://doi.org/10.1103/physrevfluids.8.024607

Solodoch, A., Barkan, R., Verma, V., Gildor, H., Toledo, Y., Khain, P., & Levi, Y. (2023). Basin-scale to submesoscale variability of the east mediterranean sea upper circulation. *Journal of Physical Oceanography*, *53*(9), 2137–2158. https://doi.org/10.1175/jpo-d-22-0243.1

Srinivasan, K., Barkan, R., & McWilliams, J. (2023). A forward energy flux at submesoscales driven by frontogenesis. *Journal of Physical Oceanography*, *53*(1), 287–305. https://doi.org/10.1175/jpo-d-22-0001.1

Sundermeyer, M. A., Birch, D. A., Ledwell, J. R., Levine, M. D., Pierce, S. D., & Cervantes, B. T. K. (2020). Dispersion in the open ocean seasonal pycnocline at scales of 1-10 km and 1-6 days. *Journal of Physical Oceanography*, *49*(2), 415–437. https://doi.org/10.1175/jpo-d-19-0019.1

Tchilibou, M., Gourdeau, L., Morrow, R., Serazin, G., Djath, B., & Lyard, F. (2018). Spectral signatures of the tropical pacific dynamics from model and altimetry: A focus on the meso/submesoscale range. *Ocean Science*, *14*(5), 1283–1301. https://doi.org/10.5194/os-14-1283-2018

Tedesco, P., Baker, A., Naveira Garabato, L. E., Mazloff, M., Gille, S., Caulfield, C., & Mashayek, A. (2024). Spatiotemporal characteristics of the near-surface turbulent cascade at the submesoscale in the drake passage. *Journal of Physical Oceanography*, *54*(1), 187–215. https://doi.org/10.1175/jpo-d-23-0108.1

Thomas, J. (2023). Turbulent wave-balance exchanges in the ocean. *Proceedings of the Royal Society A: Mathematical, Physical and Engineering Sciences*, *479*(2276), 20220565. https://doi.org/10.1098/rspa.2022.0565

Thomas, J., & Arun, S. (2020). Near-inertial waves and geostrophic turbulence. *Physical Review Fluids*, *5*(1), 014801. https://doi.org/10.1103/physrevfluids.5.014801

Thomas, J., & Daniel, D. (2021). Forward flux and enhanced dissipation of geostrophic balanced energy. *Journal of Fluid Mechanics*, *911*, A60. https://doi.org/10.1017/jfm.2020.1026

Thomas, J., & Gupta, A. (2022). Wave-enhanced tracer dispersion. *Journal of Geophysical Research: Oceans*, *127*(3), e2020JC017005. https://doi.org/10.1029/2020jc017005

Thomas, J., & Vishnu, R. (2022). Turbulent transition of a flow from small to O(1) Rossby numbers. *Journal of Physical Oceanography*, *52*(11), 2609–2625. https://doi.org/10.1175/jpo-d-21-0270.1

Thomas, J., & Yamada, R. (2019). Geophysical turbulence dominated by inertia-gravity waves. *Journal of Fluid Mechanics*, *875*, 71–100. https://doi.org/10.1017/jfm.2019.465

Thompson, A. F., Lazar, A., Buckingham, C. E., Naveira Garabato, A. C., Damerell, G. M., & Heywood, K. J. (2016). Open-ocean submesoscale motions: A full seasonal cycle of mixed layer instabilities from gliders. *Journal of Physical Oceanography*, *46*(4), 1285–1307. https://doi.org/10.1175/jpo-d-15-0170.1

Torres, H. S., Klein, P., Menemenlis, D., Qiu, B., Su, Z., Wang, J., et al. (2018). Partitioning ocean motions into balanced motions and internal gravity waves: A modeling study in anticipation of future space missions. *Journal of Geophysical Research: Oceans*, *123*(11), 8084–8105. https://doi.org/10.1029/2018jc014438

Vallender, S. S. (1974). Calculation of the wasserstein distance between probability distributions on the line. *Theory of Probability & Its Applications*, *18*(4), 784–786. https://doi.org/10.1137/1118101

Vallis, G. K. (2006). *Atmospheric and oceanic fluid dynamics*. Cambridge University Press.

Villani, C. (2009). *Optimal transport: Old and new* (Vol. 338). Springer.

Vladoiu, A., Lien, R., & Kunze, E. (2024). Energy partition between submesoscale internal waves and quasigeostrophic vortical motion in the pycnocline. *Journal of Physical Oceanography*, *54*(6), 1285–1307. https://doi.org/10.1175/jpo-d-23-0090.1

Wang, J., Flierl, G. R., LaCasce, J. H., McClean, J. L., & Mahadevan, A. (2013). Reconstructing the ocean's interior from surface data. *Journal of Physical Oceanography*, *43*(8), 1611–1626. https://doi.org/10.1175/jpo-d-12-0204.1

Xiao, Q., Balwada, D., Jones, S. C., Herrero-González, M., Smith, S. K., & Abernathey, R. (2023). Reconstruction of surface kinematics from sea surface height using neural networks. *Journal of Advances in Modeling Earth Systems*, *15*(10), e2023MS003709. https://doi.org/10.1029/2023ms003709

Yassin, H., & Griffies, S. M. (2022). Surface quasigeostrophic turbulence in variable stratification. *Journal of Physical Oceanography*, *52*(12), 2995–3013. https://doi.org/10.1175/jpo-d-22-0040.1

Yu, X., Naveira Garabato, A. C., Martin, A. P., Buckingham, C. E., Brannigan, L., & Su, Z. (2019). An annual cycle of submesoscale vertical flow and restratification in the upper ocean. *Journal of Physical Oceanography*, *46*(6), 1439–1461. https://doi.org/10.1175/jpo-d-18-0253.1

Yu, X., Ponte, S., Elipot, A. L., Menemenlis, D., Zaron, E. D., & Abernathey, R. (2019). Surface kinetic energy distributions in the global oceans from a high-resolution numerical model and surface drifter observations. *Geophysical Research Letters*, *46*(16), 9757–9766. https://doi.org/10.1029/2019gl083074

Zeitlin, V., Reznik, G. M., & Ben, J. (2003). Nonlinear theory of geostrophic adjustment. Part 2. two-layer and continuously stratified primitive equations. *Journal of Fluid Mechanics*, *491*, 207–228. https://doi.org/10.1017/s0022112003005457